



저작자표시-비영리-변경금지 2.0 대한민국

이용자는 아래의 조건을 따르는 경우에 한하여 자유롭게

- 이 저작물을 복제, 배포, 전송, 전시, 공연 및 방송할 수 있습니다.

다음과 같은 조건을 따라야 합니다:



저작자표시. 귀하는 원저작자를 표시하여야 합니다.



비영리. 귀하는 이 저작물을 영리 목적으로 이용할 수 없습니다.



변경금지. 귀하는 이 저작물을 개작, 변형 또는 가공할 수 없습니다.

- 귀하는, 이 저작물의 재이용이나 배포의 경우, 이 저작물에 적용된 이용허락조건을 명확하게 나타내어야 합니다.
- 저작권자로부터 별도의 허가를 받으면 이러한 조건들은 적용되지 않습니다.

저작권법에 따른 이용자의 권리는 위의 내용에 의하여 영향을 받지 않습니다.

이것은 [이용허락규약\(Legal Code\)](#)을 이해하기 쉽게 요약한 것입니다.

[Disclaimer](#)

의학석사 학위논문

Three-Dimensional Visualization and  
Quantification of the Whole Enteric  
Nervous System in Mouse and Human  
using Tissue Clearing

조직 투명화를 이용한 쥐와 사람의 전체  
장신경계 3차원 시각화 및 정량화

2021년 2월

서울대학교 대학원

의학과 해부학전공

윤영현

A Thesis of the Degree of Master of Philosophy

Three-Dimensional Visualization and  
Quantification of the Whole Enteric  
Nervous System in Mouse and Human  
using Tissue Clearing

조직 투명화를 이용한 쥐와 사람의 전체  
장신경계 3차원 시각화 및 정량화

February 2021

Department of Anatomy & Cell Biology

Graduate School of Medicine

Seoul National University

Young Hyun Yun

조직 투명화를 이용한 쥐와 사람의 전체  
장신경계 3차원 시각화 및 정량화

지도교수 황 영 일

이 논문을 의학석사 학위논문으로 제출함

2020년 10월

서울대학교 대학원

의학과 해부학전공

윤 영 현

윤영현의 의학석사 학위논문을 인준함

2021년 1월

위원장 최형진 (인)  
부위원장 김성애 (인)  
위원 고병진 (인)

Three-Dimensional Visualization and  
Quantification of the Whole Enteric  
Nervous System in Mouse and Human  
using Tissue Clearing

by

Young Hyun Yun

A Thesis Submitted to the Department of  
Anatomy & Cell Biology in Partial Fulfillment of the  
Requirements for Master Degree in Medicine at Seoul  
National University College of Medicine

January 2021

Approved by thesis committee:

Professor Choi, Hyung-Jin Chairman

Professor Hwang, Young-il Vice Chairman

Professor Ko, Seong-Joon

## Abstract

# Three–Dimensional Visualization and Quantification of the Whole Enteric Nervous System in Mouse and Human using Tissue Clearing

Young Hyun Yun

Department of Medicine

The Graduate School

Seoul National University

**BACKGROUND & AIMS:** Nowadays, state-of-the-art tissue clearing methods enable visualization of the thicker tissue section or even whole organ imaging, by increasing tissue transparency and enhancing the antigen–antibody reaction. The goal of this research was to establish a 3D imaging method for the whole gastrointestinal (GI) tract that yields more information and insight about the enteric nervous system (ENS) than traditional 2D tissue section imaging. This approach will improve a comprehensive understanding of research purpose and diagnosis of human diseases, such as

Hirschsprung disease, bowel motility disorders, or inflammatory bowel disease (IBD). The present study optimized a technique to image transgenic fluorescence mice and human ENS that express fluorescent neuron-specific class III beta-tubulin (Tuj1), neuronal nitric oxide synthase (nNOS), choline acetyltransferase (ChAT), and RNA binding proteins (HuC/D) in 3 dimensions.

**METHODS:** Visualization and quantification of the digestive organs (e.g. esophagus, stomach, small intestine, and colon) in mice and humans were carried out through various techniques. A method, encompassing tissue clearing, immunohistochemistry (IHC), confocal microscopy, light sheet fluorescence microscopy (LSFM), and quantitative analysis of full-thickness bowel without tissue sections, had been established for 3D imaging at high resolution. Furthermore, using surface rendering, volume rendering for all channels, fluorescence thresholding, and background subtraction, tools from in IMARIS, cleared tissues could be visualized in an accurate 3D structure.

**RESULTS:** The multiscale structural decomposition of mouse and human ENS was clearly visualized in 3D. The tissue clearing method could image the complex ENS network structure of myenteric plexus, submucosal plexus, and mucosal nerves. Similarly, the 3D ENS

network structure of the esophagus ( $16 \times 14 \times 5.3$  mm) and colon ( $1.2 \times 1.3 \times 1.4$  mm) samples were visualized in mouse and human, respectively. I investigated the cholinergic ENS structure through the whole GI tract and quantified the number of cell bodies and cell bodies per ganglion in myenteric and submucosal plexus in mouse ( $n=3$ ). To identify the hubness of the myenteric plexus in mouse, I measured the number of ganglia and bridges without cell bodies that connected the ganglion. Quantitative data for myenteric plexus and submucosal plexus showed relatively different aspects.

**CONCLUSIONS:** This study was the first to visualize the mouse and human whole ENS in three dimensions with no sectioning and microanatomy. The cytoarchitecture of the mouse tissues could be quantitatively analyzed, preserving the tissue structure, and providing more accurate data with tissue clearing. A quantitative analysis method of structure phenotypes in mouse will illuminate the potential usefulness of this technology. For GI motility disorders, this novel technology will unravel the extensive spatial 3D network structure of neuro-immune interaction.

---

**Keywords:** Tissue clearing, Enteric nervous system, Myenteric plexus, Submucosal plexus, Three-dimensional structure

**Student number:** 2019-20007

# Contents

Abstract	i
Contents	iv
List of tables	v
List of figures	vi
List of abbreviations	ix
Introduction	1
Materials and Methods	6
Results	11
Discussion	21
References	26
Abstract (Korean)	70

## List of tables

**Table 1.** Antibodies used for immunohistochemistry \_\_\_\_\_ 30

**Table 2.** The types of antibodies used in each organ of the  
mouse and human \_\_\_\_\_ 31

## List of figures

<b>Figure 1.</b> The organization and multiscale frame of the enteric nervous system _____	32
<b>Figure 2.</b> Macroscale and mesoscale of esophagus ENS in mouse _____	34
<b>Figure 3.</b> Full-thickness and microscale of esophagus ENS in mouse and human _____	36
<b>Figure 4.</b> Macroscale and mesoscale of stomach ENS in mouse _____	38
<b>Figure 5.</b> Mesoscale and microscale of stomach ENS in mouse _____	40
<b>Figure 6.</b> Full-thickness and microscale of stomach ENS in human _____	42
<b>Figure 7.</b> Microscale of stomach ENS in human _____	45

<b>Figure 8.</b>	Macroscale and mesoscale of small intestine ENS in mouse _____	48
<b>Figure 9.</b>	Mesoscale and full thickness of small intestine ENS in mouse _____	50
<b>Figure 10.</b>	Full-thickness and microscale of small intestine ENS in mouse _____	52
<b>Figure 11.</b>	Microscale of small intestine ENS in human _____	54
<b>Figure 12.</b>	Macroscale and mesoscale of colon ENS in mouse _____	56
<b>Figure 13.</b>	Microscale of colon ENS in mouse _____	58
<b>Figure 14.</b>	Full-thickness of sigmoid colon ENS in a patient with Crohn's disease _____	60
<b>Figure 15.</b>	Microscale of sigmoid colon ENS in human _____	62

- Figure 16.** Histology illustration of small intestine and colon in ChAT reporter mouse \_\_\_\_\_ 64
- Figure 17.** Distance between two major plexus and quantification of cholinergic neurons in submucosal plexus \_\_\_\_ 66
- Figure 18.** Quantification of cholinergic neurons in myenteric plexus \_\_\_\_\_ 68

## List of abbreviations

**ANS:** Autonomic nervous system

**CD:** Crohn's disease

**ChAT:** Choline acetyltransferase

**CNS:** Central nervous system

**DSS:** Dextran sulfate sodium

**ENS:** Enteric nervous system

**ETC:** Electrophoretic tissue clearing

**GI:** Gastrointestinal

**H&E:** Hematoxylin and Eosin

**IBD:** Inflammatory bowel disease

**IHC:** Immunohistochemistry

**LSFM:** Light sheet fluorescence microscopy

**MP:** Myenteric plexus

**nNOS:** Neuronal nitric oxide synthase

**PBS:** Phosphate-buffered saline

**SMP:** Submucosal plexus

**SPIM:** Selective plane illumination microscopy

**UC:** Ulcerative colitis

**VAcHT:** Vesicular acetylcholine transporter

# Introduction

The gastrointestinal (GI) system, also referred to as the GI tract or gut, contains its own nervous system that operates independently of the brain and spinal cord, the enteric nervous system (ENS). The ENS is a division of the autonomic nervous system (ANS) and consists of a web-like neural structure that regulates many GI functions, the other divisions being sympathetic and parasympathetic in vertebrates [1, 2]. Recently, it has been known that alterations of the ENS structures and control of neural activity are involved in regulating the intestinal inflammatory response through neuro-immune interaction [3]. Also, disorders of GI motility may result from qualitative or quantitative abnormalities of the ENS [4–7]. Hence, structural damage to the ENS causes a variety of disorders, including but not limited to Hirschsprung disease, diarrhea, or inflammatory bowel diseases (IBD) including Crohn's disease (CD) and ulcerative colitis (UC) [8].

There are two major types of plexus within the GI tract which are called the myenteric (Auerbach's) plexus and the submucosal (Meissner's) plexus. The myenteric plexus which is located between the inner circular, and outer longitudinal muscle layers, and

the submucosal plexus which is situated in the submucosal region have become an important issue in reflex pathway for the past two decades [9]. Enteric neurons are arranged in two interconnected networks (myenteric and submucosal plexus) that extend from the esophagus to the anal verge [10]. In the small and large intestine, the ganglionated plexuses exist in the submucosa, whereas it is absent from the esophagus and almost no submucosal ganglia are present in the stomach. Also, the organization and the differences between regions of the GI tract and species have been reviewed [1, 10, 11]. To regulate GI motility and to coordinate motor activity such as peristalsis and the migrating motor complex over longer distances, interneurons communicate with each other and with motor neurons. During peristalsis, excitatory and inhibitory motor neurons are needed to contract or relax smooth muscle, respectively [6].

Due to its relatively chaotic architecture, specific functions of circuit elements are yet to be fully distinguished. Acetylcholine, synthesized by choline acetyltransferase (ChAT), is the most major excitatory neurotransmitter, while nitric oxide, synthesized by neuronal nitric oxide synthase (nNOS), is a common inhibitory neurotransmitter [12]. Thus, mutually exclusive secretomotor neurons can be characterized by immunofluorescent antibody markers targeting either enzyme which is expressed in 95% of the ENS neurons [12].

Guinea pig and mouse neuron type identities were finally established about 20 years ago [13, 14]. The size and thin thickness of the murine GI tract enabled whole-mount studies, as well as the use of transgenic mouse, and which helped omit staining processes [15]. With proper combination of antibodies, including those targeting nNOS, ChAT, vesicular acetylcholine transporter (VACHT), and calretinin, and 90% of myenteric neurons could be identified [12, 16]. On the other hand, how the properties of murine submucosal neurons correlate and how it varies along the gut remains elusive. Regional differences highlight corresponding functional differences [17].

Several studies have demonstrated that ENS structures are easily visualized in mice via whole-mount immunostaining because the murine bowel is very thin [12, 18]. In contrast, visualizing human ENS is challenging because of the high amounts of extracellular matrix [19]. For these reasons, most studies using human tissue samples rely primarily on thin sections to be visualized the ENS, and therefore the ENS structures are only examined locally without a cleared neural network. The main problem is that the major ENS structures such as the submucosal and myenteric plexus were difficult to appreciate in sectioned organ and even if you saw the ENS structure well, 3D ENS imaging provided only a limited perspective of the neural network [3].

While seeming sufficient in identifying neuron types and populations, the previous two-dimensional imaging techniques have certain fundamental limitations. The first is that as imaging frames are quite small to be counted ganglia, a region of the tissue samples is randomly selected. This causes marked fluctuations in neuron counting and density. Second, it is well known that neural density differs along with the depth and length; for instance, there is a gradient along the murine colon in the total number of ganglia as well as the proportion of cholinergic neurons [20]. Such regional differences are often overseen and uncounted for. Lastly, as whole-mount studies usually section submucosa and mucosa or muscle layers, the plexuses can only be studied separately. Thus, a holistic understanding of the innervation and fiber structure spanning the whole thickness of the guts is difficult to construe. While the ENS carries out functions independent of the central nervous system, normally it receives influences from central nervous system (CNS) and sends information to the brain. A robust gut-brain connection is crucial to gut function such as visceral motor control for a bowel movement and visceral sensory (mechano-sensory and chemo-sensory) [21]. The innervation structure can only be fully understood through full-thickness imaging, as the neurons penetrate the longitudinal and circular muscle layers. Total removal of the

innervation structure hampers a thorough understanding of the network.

Overall, this study provides an alternative to previous imaging techniques. I established a stable method to observe three-dimensional ENS in large regions without tissue sections via confocal microscopy and light sheet fluorescence microscopy (SPIM). Respective protocols for mouse and human ENS were applied for the esophagus to the colon. Images of various scopes from microscopic to full-thickness to a mesoscopic and macroscopic level were taken.

# Material and Methods

## Mice

The study was conducted by using male ChAT-Cre tdTomato mice (8–12-weeks-old) and male Wild-type (WT) mice (8–12 weeks-old). The animal care and handling protocols were performed with the approval of the Institutional Animal Care and Use Committee (IACUC) of Seoul National University College of Medicine (IACUC No. 17-0166-c1a1). All mice were fed and housed under temperature-controlled room ( $23 \pm 2^\circ\text{C}$ ) with light/dark cycles (12 hours/12hours; T = 24 hours).

## Human Tissue

### Human autopsy specimen

Human tissue samples were obtained during autopsies. With approval from the Institutional Review Board for Human Subjects Research at Seoul National University (No. 2020-008), autopsied human specimen (e.g. esophagus, fundus, body, antrum, small intestine, and colon) were collected by certified staff in the Department of Forensic Medicine of the Seoul National University (Seoul, Korea) following the standard operating procedure for autopsies.

## **Biopsy and surgical tissues from patients**

Human GI tissue samples (e.g. fundus, body, and antrum) were obtained from patients between 20 and 65 years old who had diabetes mellitus at Seoul National University Bundang Hospital (SNUBH) during sleeve gastrectomy, sleeve gastrectomy with proximal jejunal bypass, and sleeve gastrectomy with duodenojejunal bypass. Colon samples were from Seoul National University Hospital (SNUH) during a colonoscopy (IRB No. H-0603-071-170).

## **Tissue Processing**

### **Mice**

All mice were anesthetized with Ketamine (140 mg/kg<sup>-1</sup> I.P.) and sacrificed by transcardial perfusion with 1× phosphate-buffered saline (PBS) and 4% paraformaldehyde (PFA). After 5 minutes of continuous perfusion, organs (e.g., esophagus, stomach, small intestine, and colon) were harvested and fixed (4% paraformaldehyde, 4°C, overnight). The fixed tissues were then washed in 1× PBS (room temperature, on a shaker, overnight).

### **Human Tissue**

Human tissues such as the esophagus, stomach, small intestine, and colon were immediately cut 1×1 cm<sup>2</sup> with laser blade and then

washed with  $1 \times$  PBS to remove fat. The tissues were put in ice-cold 4% PFA and carried to the laboratory in an icebox. After fixed (4% PFA, 4°C, overnight), the tissues were washed (PBS, overnight, room temperature) and transferred to 0.3% hydrogen peroxide ( $H_2O_2$ ) to eliminate some of the red blood cells before staining.

## **Tissue clearing**

To clear tissue samples, the fixed tissue samples were incubated in Electrophoretic Tissue Clearing (ETC) Solution (Cat No. C13001) which was made up of 200 mM boric acid, and 4% (wt/vol) SDS (pH 8.5). In ETC mode, platinum-plated electrodes make an electric field to accelerate the removal of lipids from tissues in the most efficient manner. Human tissue samples took at least 20 hours in ETC mode and were incubated in ETC solution on a shaker (3 days, 60°C, 70 rpm) for further removed of the lipid. Mice tissue samples were transferred into the cassette for the ETC chamber for about 4 hours and then incubated in ETC solution on a shaker (2 hours, 60°C, 70 rpm).

## **Immunohistochemistry**

The experiment was conducted using DeepLabel™ Antibody Staining Kit (Cat No. C33001). After washed cleared tissue samples with  $1 \times$

PBS for 24 hours, tissue samples were immersed in DeepLabel™ Solution A to enhance antibody penetration into clarified tissues. The transparent samples were then incubated with primary antibodies diluted in DeepLabel™ Solution B for 2–3 days. The primary antibodies used in mouse and human were chicken anti- $\beta$  III tubulin IgY (1:500; neuromics, CH23005), chicken anti- $\beta$  III tubulin (1:500; Novus Biologicals, NB100-1612), sheep anti-choline acetyltransferase (1:500; abcam, ab18736), goat anti-nNOS (neuronal) (1:500; abcam, ab1376) or rabbit anti-HuC/D (1:500; abcam, ab237235). The samples were then washed three times with DeepLabel™ Washing Buffer, and incubated with secondary antibodies diluted in DeepLabel™ Solution B for 2–3 days. The secondary antibodies used in this study were donkey anti-goat IgG H&L 350 (1:500, Invitrogen, a21081), donkey anti-chicken IgG H&L 488 (1:500, Invitrogen, a11039), and donkey anti-sheep IgG H&L 594 (1:500 abcam, ab150180). DeepLabel™ Washing Buffer was used after primary and secondary staining. To minimize photobleaching and preserve fluorescence signals, tissues were then incubated in enough X-CLARITY™ Mounting Solution for one day. The duration of each step depended on the size of the tissue samples. The human tissue samples usually took about a day longer than the mouse samples. All steps were performed at 37°C in dark with gentle shaking.

## **Imaging**

All imaging of immunohistochemistry (IHC) specimens was performed on the C2 upright confocal microscopy (10× objective, Nikon Instruments, Yokohama, Japan), Leica TCS SP8 CARS confocal microscopy (Leica Microsystems GmbH, Wetzlar, Germany), and a selective plane illumination microscopy (LaVision Biotec, Bielefeld, Germany) at the Biomedical Imaging Center in Seoul National University College of Medicine. The images were acquired by confocal microscopy using the laser excitation wavelengths of 350 nm, 488 nm, 594 nm, or 647 nm. Confocal images were carried out using ImageJ (National Institutes of Health) for cell counting.

## **Statistical analysis**

Different regions of the mouse small intestine and colon were quantified using one-way ANOVA. Multiple pairwise comparisons were performed using post hoc Tukey's multiple comparison test. The statistical significance was expressed with the following symbols: (\*  $P < 0.05$ ), (\*\*  $P < 0.01$ ), (\*\*\*)  $P < 0.001$ ), and (\*\*\*\*  $P < 0.0001$ ), to indicate statistical differences. All analyses were conducted with Microsoft Excel and GraphPad Prism7.

# Results

## Visualization of the mouse and human ENS in three dimensions

### A multiscale framework of ENS in mouse and human

Fig 1A shows the organization of the ENS of human and medium-large mammals [22]. All images in this study followed a multiscale framework of the ENS in both mouse and human tissue samples. Representative results of confocal images using tissue clearing are shown in Fig 1B. Three-dimensional images of mouse whole GI tract could be obtained at different levels such as macroscale, mesoscale, full-thickness, and microscale. Macroscale is in the level of the whole body, and mesoscale is used to define organs. Full-thickness is an intermediate level between mesoscale and microscale. The difference between full-thickness and microscale is that the former shows the entire network structure of ENS from the mucosa to serosa, and the latter can be quantitatively analyzed. As human specimens are considerably larger than murine gut samples, tissue clearing for the entire body and whole organ was one of the major obstacles. To achieve the scalable clearing of human tissue samples, I only considered full-thickness scale/level and imaged parallel to bowel surface.

## Visualization of esophagus ENS in mouse and human

Cholinergic neurons in the esophagus were visualized using a ChAT reporter mouse. All panels are light sheet fluorescence microscopy (SPIM) images of the mouse esophagus, and three-dimensional confocal images exhibited the cytoarchitecture in sharp detail (Fig 2). The inner cholinergic neurons seem to have a very tight spiral that the windings are virtually circular, whereas the outer one seems to have a very slowly unwinding spiral that the windings are virtually longitudinal (Fig 2C).

Furthermore, I visualized the mice and human ENS in the esophagus using the tissue clearing method and compared this observation to the Hematoxylin and Eosin (H&E) stain. The ENS was difficult to observe in cross-sections of the human esophagus (Fig 3A). In contrast, the tissue clearing method showed the ENS structure well. In the mouse, the esophagus had a rich network of thin nerve fibers that run along with the thick nerve fiber (Fig 3A, B). The esophagus had a thick bundle of nerve fibers in the outer layer of the esophagus, and a neural network of thin nerve fibers are situated above the thick nerve fibers. Also, partial-thickness from the mucosa to the submucosa of the human esophagus stained for Tuj1 and DAPI was imaged in three dimensions (Fig 3A, C). Figure 3C represents two

layers, an inner circular and an outer longitudinal muscle layer between the submucosa and serosa.

### **Visualization of stomach ENS in mouse and human**

SPIM allowed the investigation of long-range neuronal connections spanning the mouse whole stomach. CLARITY-processed mouse stomach was stained with Tuj1 antibody (green) to reveal the fine details of axons and their terminations (Fig 4A). Complete transparency enabled visualization of intact stomach tissue in different angles of view that had not been observed in thin tissue sections (Fig 4B). Zoom-in images of different regions from the mouse stomach are shown in Fig 4C. A rich network of thick nerve fibers is located near the esophagus region and extends all over the stomach.

To compare the ENS structures of the gastric fundus, body, and antrum, the mouse stomach was stained for Tuj1 (red) and was imaged parallel to the bowel surface. One hundred forty-four tiles (1 tile =  $1024 \times 1024 \mu\text{m}$ ) of confocal Z-stacks images were obtained and then the tiles were stitched forming the complete image in 2D (Fig 5A is  $12.6 \times 12.6 \text{ mm}$ ). Nerve fibers within the ENS consist of the axons of enteric neurons that project to the gut wall. I investigated three main regions in the stomach; fundus, body, and

antrum (Fig 5B, C, D). The ganglionated submucosal plexus was absent from the fundus to the antrum and contained only very few ganglia in the stomach. But, there were some differences in structure, depth, and organization between regions of the stomach. In the fundus of the stomach, some star-like structures were strung together by ChAT positive neurons in nerve fibers, and some were closely adherent to other ganglia. Also, the gastric wall of the antrum was the thickest of the other regions of the stomach. In the gastric body, the thickness of nerve fibers was approximately 10  $\mu\text{m}$  which was thinner than those in the gastric fundus and antrum.

I compared the structure of ENS neurons in two dimensions (H&E stain) with the 3D ENS structure of the human fundus (Fig 6A). The ENS is difficult to appreciate in a cross-section image likewise H&E stained section image of the esophagus. Microscale of the human stomach from mucosa to serosa and submucosa to serosa was visualized in three dimensions. The different morphologies of the ENS network in different layers of the gut wall were visualized in dissect layers from outside (blue) to inside (yellow) using a depth coding approach. Previous studies have reported that the gastric muscularis externa is a smooth muscle located in the submucosa and made up of 3 layers; oblique, inner circular, and outer longitudinal [23]. However, the oblique muscle layer of the fundus could not be

distinguished based on the histological characteristics (Fig 6B). The nerve fibers in the myenteric plexus seemed to extend upward toward the mucosa layer (Fig 6C). Double-labeled image of myenteric plexus decomposed into individual fluorophores. Small clustered ganglia have NeuN (green), and Tuj1 (red), and t fibers include all cell bodies within myenteric ganglia (Fig 6D). Next, the human antrum of the stomach was stained with Tuj1 (green) and DAPI (blue) antibodies and partial-thickness from mucosa to serosa was visualized in 3D (Fig 6E). Nerve fibers in the mucosa extend down to the submucosa along with the gastric pits, and blood vessels are located in the submucosa region (Fig 6F).

Next, I attempted to clear fixed human fundus and body tissue samples with the tissue clearing method (Fig 7). Microscale of the gastric fundus was only visualized between the mucosa and submucosa (Fig 7A, B), and lower numbers of slices are closer to rugae of the mucosa. Imaging of the slices shows that the mucosa is full of gastric pits as small circular openings, and there are prominent nerve fibers near the mucosa. Also, the body of the stomach was visualized in two parts. The association between the outermost layer of the mucosa and submucosa, and between submucosa and serosa was investigated (Fig 7C–F). The inner layer of the stomach had full of wrinkles and small pores (Fig 7B, D). I observed that the nerve

fibers reach all layers from the most superficial portions of the gastric pits to the outer smooth muscle layer (Fig 7C–F). Also, the myenteric plexus was characterized by a dense network of nerve fibers that are interposed into many ganglions (Fig 7E).

### **Visualization of small intestine ENS in mouse and human**

Macroscale and mesoscale of ChAT reporter mouse small intestine ENS were visualized in three dimensions (Fig 8A). Tissue cleared small intestine maintained its native in situ cytoarchitecture, allowing visualization of distinct histological structures and their neural network. Cholinergic neurons were visible in the deep mucosal layer, and their arrangement within the cylinder-shaped villi became readily when the volume was rotated to the appropriate orientation (Fig 8B).

Mesoscale and full-thickness of transgenic mouse small intestine were visualized (Fig 9A). Three-dimensional reconstruction exhibits the small intestine cytoarchitecture in sharp detail from mucosa to serosa. (Fig 9B, C). Especially full-thickness images of the small intestine make it easy to identify the dominating myenteric and submucosal plexus, which allowed for detailed visualization of the branching pattern of two major ganglionated plexus as well as fine fibers in the villi. Besides, full-thickness and microscale of the small

intestine were imaged and stained with Tuj1 (green) in the ChAT reporter mouse (Fig 10A).

The mucosal villi of the small intestine were visualized in human samples (Fig 11). The villi project into the intestinal cavity, and Tuj1-positive (green) and nNOS-positive (red) nerve fibers are present within the villi, showing the enteric network within the small intestine. Fig 11B shows that nerve fibers in the villi do not extend to the end of the villi. Fig 12C shows a horizontal cross-sectional view of villi, and nerve fibers are gathered within the villi.

### **Visualization of colon ENS in mouse and human**

Three-dimensional reconstruction of optically cleared mouse colon was visualized in 3D (Fig 12A). The optimized protocol describes here enables the colon to be visualized in more detail than previously possible using 2D approaches. The 3D images showed a ganglionated plexus and nerve fibers innervated to the mucosa. In microscale, the colon ENS of ChAT reporter mouse was shown by immunofluorescent double staining (Fig 13). The nerve meshes and the distribution of ganglia were arranged densely in the myenteric plexus. Also, the myenteric plexus was composed of ganglia and interconnecting nerve fibers forming a polygonal network; however, the submucosal plexus was not ganglionated and contained isolated

nerve cell bodies. Inner circular muscle layers contained thin nerve fibers (Fig 13C).

Full-thickness of sigmoid colon ENS in patients with Crohn's disease was visualized in three dimensions (Fig 14A). Each image represents Tuj1-positive neurons and nNOS-positive neurons in the sigmoid colon. Antibody staining against the neuronal marker Tuj1 impressively revealed the structure of the myenteric plexus, submucosal plexus, and fine nerve fibers running within the muscle layers. Although I could characterize it by a colon wall with four layers, changes in the morphology of the ENS was observed in a CD patient. In submucosa, a patient with CD showed the existence of ENS abnormalities including nerve trunks of increased size (Fig 14B). I also found that the nerve fibers include all cell bodies (NeuN) within myenteric ganglia (Fig 14C) and thickening of the inner circular muscle layer as well as muscularis mucosa within the submucosa itself have been observed.

Microscale of the human sigmoid colon from submucosa to serosa was imaged and stained with pan-neuronal marker, Tuj1 antibody (Fig 15A). Cleared human sigmoid colon samples maintained the native intestinal cytoarchitecture, allowing visualization of distinct histological layers and their transitions. Tuj1 staining of the human

sigmoid colon reveals elongated neuron fibers and axons of the inner circular and the outer longitudinal muscle layer. The submucosal layer transitions into a serosa layer were characterized by prominent autonomic neural fibers and ganglionic clusters that form the myenteric plexus (Fig 15B).

### **Quantification of cholinergic neurons in the reporter mouse small intestine and colon**

The majority of the myenteric neurons in the small intestine and colon contain either ChAT or nNOS, and the number of these neurons was approximately the same in the reporter mouse and immunostaining method in the wild type mouse [12]. Therefore, I quantified the number of cholinergic neurons in the small intestine and colon using ChAT-Cre tdTomato mouse (n=3). Next, I asked how the ENS structures over a distance impact neuron density estimates, recognizing that ENS is not uniformly distributed. To solve this, I performed an analysis for the quantification of cholinergic neurons in the small intestine and colon of mice. Fig 14 shows the distance-related morphological changes in the submucosal and myenteric plexus along the mouse small intestine and colon.

The distance between the submucosal and myenteric plexus was similar in proximal and middle small intestine and significantly

increased from middle small intestine to colon (Fig 15A, B). In the submucosal plexus, the number of cell bodies per 1.61 mm<sup>2</sup> was significantly decreased as it moves from the beginning of the small intestine to the end of the colon (Fig 15D). Thus, there was a significantly higher number of cell bodies per 1.61 mm<sup>2</sup> in the small intestine compared with the colon (Fig 15E).

In the myenteric plexus, the number of cholinergic neuron cell bodies per 1.61 mm<sup>2</sup> was significantly increased in the proximal, middle, and distal small intestine and slightly decreased in the colon (Fig 16B). To identify the hubness of the myenteric plexus, I measured bridges that connect two or more ganglia. The number of bridges per ganglion has decreased as it moves from the middle small intestine to the end of the colon. Lastly, the number of cholinergic neuron cell bodies per 1.61 mm<sup>2</sup> showed no significant difference between the small intestine and colon.

## Discussion

The imaging approach applied in this study was the first to be scalable for 3D visualization of the mouse and human whole ENS ranging from the esophagus to colon. In addition to 3D visualization, I performed substantial quantitative analyses to investigate 3D ENS structures in the mouse small intestine and colon. For the imaging approach, four distinct scales were defined: macroscale, mesoscale, full-thickness, and microscale. Especially, tissue clearing methods and confocal microscopy provided 3D images, which enabled good visualization of the anatomy and structure of the mouse and human tissues at different length scales spanning from the macroscopic to the microscopic level. Especially, this technology made it possible to visualize the structure of the human ENS at both full-thickness and microscale and to study complex neural networks between the submucosal and myenteric plexus.

While extensive research using the tissue clearing method has been done in brain tissue, lung, pancreatic tissues, and some aspects of the intestine in the mouse, only a few studies have been reported related to human tissue samples because of some technical issues [24]. To overcome these technical problems and to achieve images of large

tissue volumes, I optimized antibody staining conditions and tissue clearing methods. According to the most recent ENS visualization study [16], visualizing human ENS took an average of one month, but the method I presented took about two weeks. Finally, with optimized image processing protocols, I achieved efficient immunostaining of human tissues with a thickness of up to 2 mm. Compared with previous studies in 3D ENS [16], this study involves a relatively larger sample imaging. Besides, I found that the transparent tissue samples derived from tissue clearing allowed penetrative confocal microscopy for an in-depth presentation of the 3D ENS structures, which could not be easily portrayed by the 2D visualization. This state-of-the-art method was not only applied to the human stomach but also the human small intestine and colon.

Next, most studies of the ENS structures were primarily visualized using 2D imaging [12, 25–27]; however, I first visualized the whole ENS using a 3D imaging system and qualitatively analyzed it. The 3D imaging provided clear spatial views of the mouse whole stomach, small intestine, and colon and revealed a complete area of interest. Three dimensional images showed the gross appearance and microstructures of the stomach, small intestine, and colon in the mouse and human and provided a more comprehensive view of the neural network, the submucosal and myenteric plexus. From these

images, the deep structures of the regions of interest in the whole-mount tissues could be visualized.

Regarding quantitative research, I carefully began to assess different regions of the mouse GI tract for the presence of neurons that contained cholinergic neurons because intestinal motility disorders may result from quantitative ENS defects [4–6]. I found some differences in the count of cholinergic neurons in the mouse small intestine and colon mouse. Based on this quantitative method, I suggest that this quantitative analysis in combination with tissue clearing methods could put forward the idea of personalizing histopathological diagnostics by quantifying neuronal subtypes. ENS structures and functions in human diseases, such as IBD, bowel motility disorder, or Hirschsprung disease, should be investigated in future studies, an area in need of additional research. The effects of age-related and bowel region on neuron density are not known. So, defining how this disease affects ENS structure, and vice versa in humans will require considerable effort, large-scale human tissue clearing, mapping intestine location, employing three-dimensional imaging, and quantitative analysis.

Several observations are worth highlighting. In the human study, a novel discovery demonstrated the presence of two layers of the

myenteric plexus between the inner circular and outer longitudinal muscle layers, which are connected (Fig 6A, C). Visualization of the gastric body on a microscale also showed that the myenteric plexus are two layers (Fig 7E, F). But, only the location of the myenteric plexus has been studied, and it is not yet known how many layers they have [12, 28, 29]. In addition, previous studies have reported that stomach is made up of three layers of smooth muscle [30], but I observed that the muscular layers consisted of smooth muscle, subdivided into the circular and longitudinal layers. I expected that the differences in these observations depend on the region of the stomach tissues based on previous stomach studies [31]. One reason is that the oblique muscle layer descends obliquely on the anterior and posterior surfaces of the stomach, where they spread out from one another and gradually disappear on the greater curvature [32]. Therefore, more studies are needed to explore the exact muscle layer of the stomach.

This study has several limitations. First, technical obstacles should be noted. The obvious limitation of this research is that large-scale human tissues remain to be a major drawback of the tissue clearing method. Especially, the human small intestine was considerably difficult to visualize in full-thickness and microscale because of the villi. To image tissue samples, they must be placed parallel to the gut

wall. In human gastric tissues, the fundus, body, and antrum were randomly oriented so I could not distinguish the exact location along the stomach. Lastly, although I successfully tested several different antibodies specific to neuronal subtypes, a few antibodies against commonly used epitopes, e.g. ChAT and HuC/D, did not show specific staining.

In summary, this study was the first to visualize the mouse and human whole GI tract ENS in three dimensions with no sectioning and microanatomy. Tissue cytoarchitecture could be quantitatively analyzed in mice, preserving the tissue structure, and providing more accurate data with tissue clearing. In the future, 3D imaging tools may provide an alternative approach to the study of the extensive spatial 3D network structure of neuro-immune interaction, thereby bridging the gap of tissue clearing methods to pathohistological diagnostic standards.

## References

1. Furness, J.B., *The enteric nervous system*. 2006, Malden, Mass.: Blackwell Pub. xiii, 274 p.
2. Furness, J.B., et al., *The enteric nervous system and gastrointestinal innervation: integrated local and central control*. *Adv Exp Med Biol*, 2014. **817**: p. 39–71.
3. Yoo, B.B. and S.K. Mazmanian, *The Enteric Network: Interactions between the Immune and Nervous Systems of the Gut*. *Immunity*, 2017. **46**(6): p. 910–926.
4. Lake, J.I. and R.O. Heuckeroth, *Enteric nervous system development: migration, differentiation, and disease*. *Am J Physiol Gastrointest Liver Physiol*, 2013. **305**(1): p. G1–24.
5. Knowles, C.H., et al., *The London Classification of gastrointestinal neuromuscular pathology: report on behalf of the Gastro 2009 International Working Group*. *Gut*, 2010. **59**(7): p. 882–7.
6. Heuckeroth, R.O., *Hirschsprung disease – integrating basic science and clinical medicine to improve outcomes*. *Nat Rev Gastroenterol Hepatol*, 2018. **15**(3): p. 152–167.
7. Uranga–Ocio, J.A., et al., *Enteric neuropathy associated to diabetes mellitus*. *Rev Esp Enferm Dig*, 2015. **107**(6): p. 366–73.
8. Lakhan, S.E. and A. Kirchgessner, *Neuroinflammation in inflammatory bowel disease*. *J Neuroinflammation*, 2010. **7**: p. 37.
9. Costa, M., S.J. Brookes, and G.W. Hennig, *Anatomy and physiology of the enteric nervous system*. *Gut*, 2000. **47 Suppl 4**: p. iv15–9; discussion iv26.

10. Brehmer, A., H. Rupprecht, and W. Neuhuber, *Two submucosal nerve plexus in human intestines*. *Histochem Cell Biol*, 2010. **133**(2): p. 149–61.
11. Brehmer, A., *Structure of enteric neurons*. *Adv Anat Embryol Cell Biol*, 2006. **186**: p. 1–91.
12. Jiang, Y., et al., *Visualizing the enteric nervous system using genetically engineered double reporter mice: Comparison with immunofluorescence*. *PLoS One*, 2017. **12**(2): p. e0171239.
13. Furness, J.B., *Types of neurons in the enteric nervous system*. *J Auton Nerv Syst*, 2000. **81**(1–3): p. 87–96.
14. Brookes, S.J., *Classes of enteric nerve cells in the guinea-pig small intestine*. *Anat Rec*, 2001. **262**(1): p. 58–70.
15. Jing, D., et al., *Tissue clearing of both hard and soft tissue organs with the PEGASOS method*. *Cell Res*, 2018. **28**(8): p. 803–818.
16. Graham, K.D., et al., *Robust, 3-Dimensional Visualization of Human Colon Enteric Nervous System Without Tissue Sectioning*. *Gastroenterology*, 2020. **158**(8): p. 2221–2235 e5.
17. Li, Z., et al., *Regional complexity in enteric neuron wiring reflects diversity of motility patterns in the mouse large intestine*. *Elife*, 2019. **8**.
18. Sang, Q., S. Williamson, and H.M. Young, *Projections of chemically identified myenteric neurons of the small and large intestine of the mouse*. *J Anat*, 1997. **190 (Pt 2)**: p. 209–22.
19. Tian, T., Z. Yang, and X. Li, *Tissue clearing technique: Recent progress and biomedical applications*. *J Anat*, 2020.

20. Foong, J.P., et al., *Properties of cholinergic and non-cholinergic submucosal neurons along the mouse colon*. J Physiol, 2014. **592**(4): p. 777–93.
21. Bai, L., et al., *Genetic Identification of Vagal Sensory Neurons That Control Feeding*. Cell, 2019. **179**(5): p. 1129–1143 e23.
22. Furness, J.B., *The enteric nervous system and neurogastroenterology*. Nat Rev Gastroenterol Hepatol, 2012. **9**(5): p. 286–94.
23. Owen, D.A., *Normal histology of the stomach*. Am J Surg Pathol, 1986. **10**(1): p. 48–61.
24. Du, H., et al., *Advances in CLARITY-based tissue clearing and imaging*. Exp Ther Med, 2018. **16**(3): p. 1567–1576.
25. Boesmans, W., et al., *Imaging neuron–glia interactions in the enteric nervous system*. Front Cell Neurosci, 2013. **7**: p. 183.
26. Barlow–Anacker, A.J., et al., *Immunostaining to visualize murine enteric nervous system development*. J Vis Exp, 2015(98): p. e52716.
27. Rao, M. and M.D. Gershon, *The bowel and beyond: the enteric nervous system in neurological disorders*. Nat Rev Gastroenterol Hepatol, 2016. **13**(9): p. 517–28.
28. Coffey, R.J., et al., *Menetrier disease and gastrointestinal stromal tumors: hyperproliferative disorders of the stomach*. J Clin Invest, 2007. **117**(1): p. 70–80.
29. Saini, N. and M. Gupta, *Morphometry of myenteric neurons in stomach*. Nepal Med Coll J, 2007. **9**(2): p. 96–9.
30. Honda, T., et al., *Mucinous bronchioloalveolar carcinoma with organoid differentiation simulating the pyloric mucosa of the stomach: clinicopathologic, histochemical,*

*and immunohistochemical analysis.* Am J Clin Pathol, 1998. **109**(4): p. 423–30.

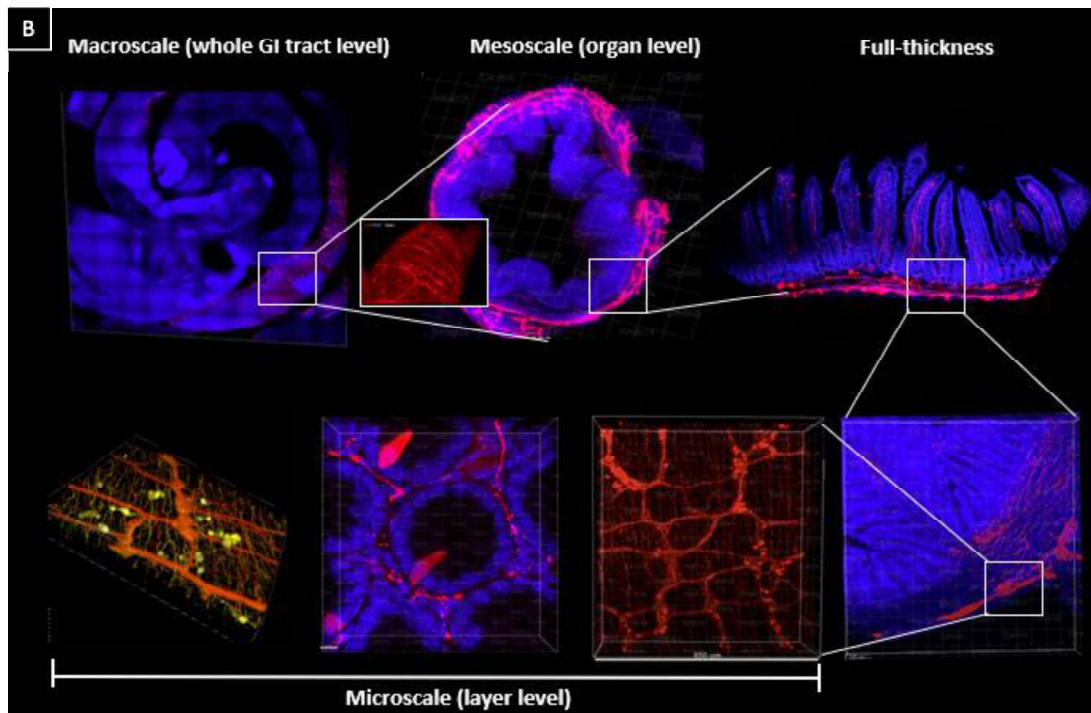
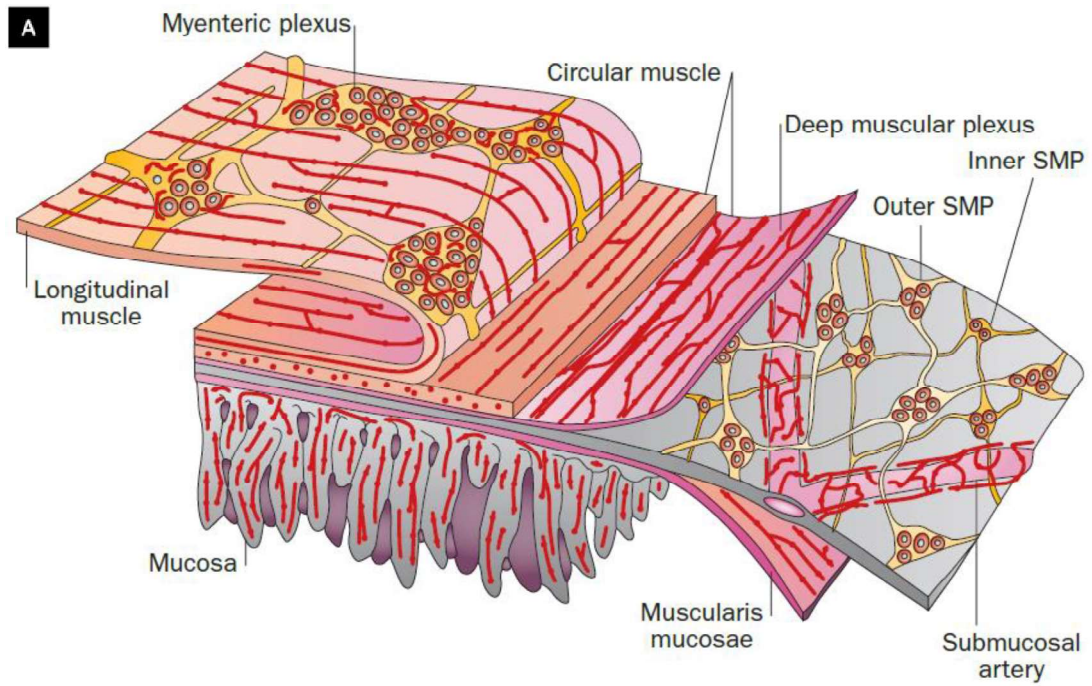
31. Peterffy, P., Sr., A. Peterffy, and P. Peterffy, Jr., [*Muscle layers of the stomach*]. Acta Chir Acad Sci Hung, 1979. **20**(2–3): p. 161–9.
32. Birmingham, A., *The Arrangement of the Muscular Fibres of the Stomach.* J Anat Physiol, 1898. **33**(Pt 1): p. 22–30.

Table 1. Antibodies used for immunohistochemistry

	Catalog #	Host	Source	Concentration
<b>Primary antibodies</b>				
Tuj1	CH23005	Chicken	neuromics	1:500
Tuj1	NB100-1612	Chicken	Novus Biologicals	1:500
ChAT	ab18736	Sheep	abcam	1:500
nNOS	ab1376	Goat	abcam	1:500
NeuN (alexa fluor 488)	MAB377X	Mouse	Sigma-Aldrich	1:200
HuC/D (alexa fluor 647)	ab237235	Rabbit	abcam	1:500
<b>Secondary antibodies</b>				
Donkey anti-chicken IgG H&L 488	a11039	Donkey	Invitrogen	1:500
Donkey anti-sheep IgG H&L 594	ab150180	Donkey	abcam	1:500
Donkey anti-goat IgG H&L 350	a21081	Donkey	Invitrogen	1:500

Table 2. Types of antibodies used in each organ of the mouse and human

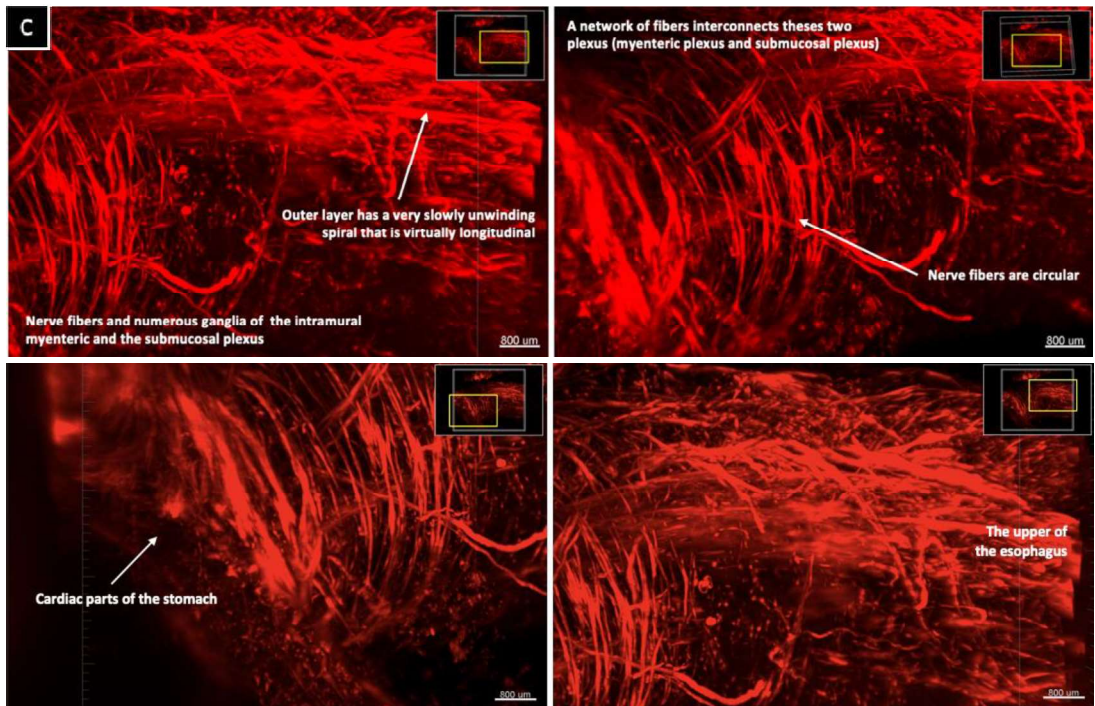
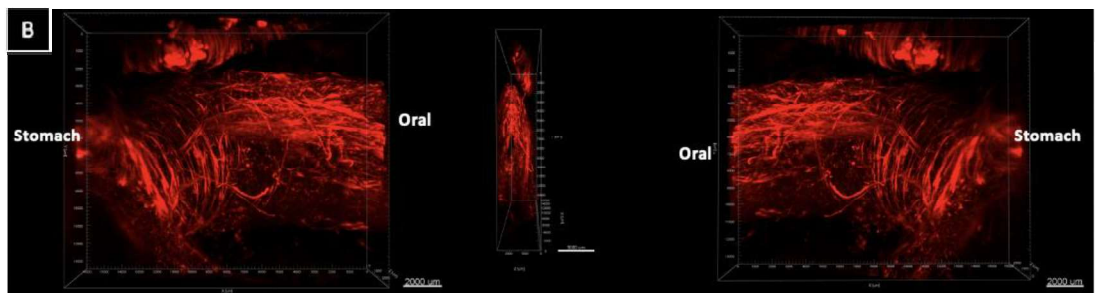
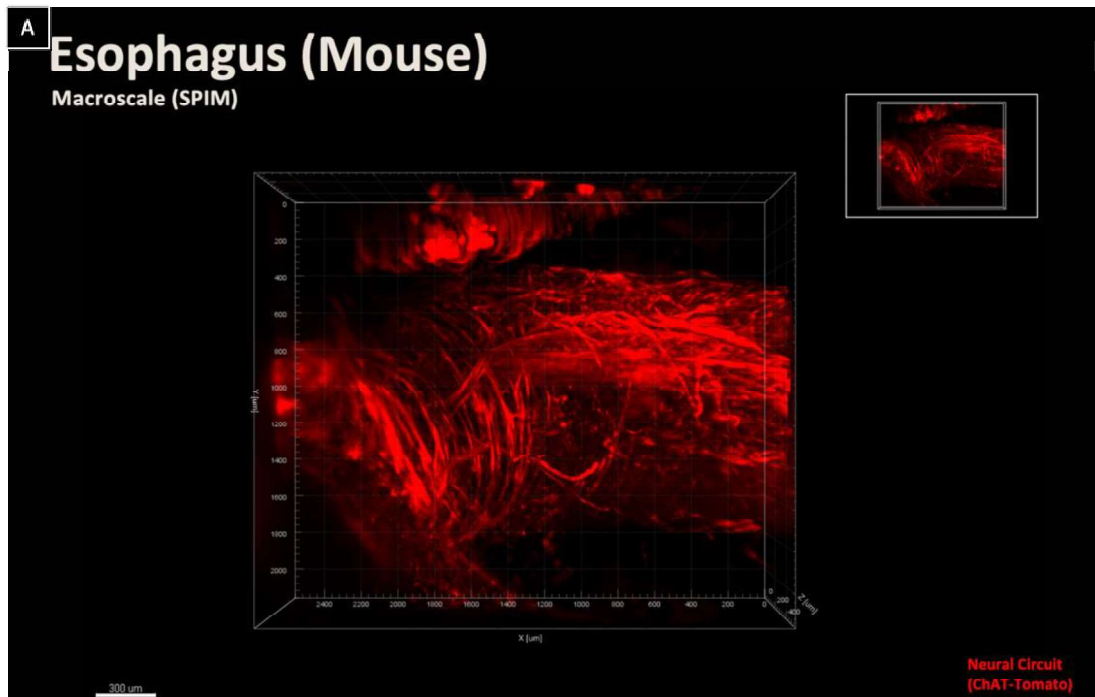
		Mouse				Human		
		Macroscale	Mesoscale	Full-thickness	Microscale	H&E stain	Full-thickness	Microscale
Esophagus		Tomato	Tomato	Tomato, DAPI	Tomato, DAPI	H&E staining	Tuj1, DAPI	x
Stomach	Fundus	Tuj1	Tuj1, DAPI	Tuj1, DAPI	Tuj1, DAPI	H&E staining	Tuj1, NeuN	Tuj1, DAPI
	Body						Tuj1, DAPI	Tuj1, DAPI
	Antrum						Tuj1, DAPI	x
Small intestine		Tomato, DAPI	Tomato, DAPI	Tomato, DAPI	ChAT Tuj1	x	x	Tuj1, nNOS
Colon		Tomato, DAPI	Tomato, DAPI	Tomato, DAPI	Tomato Tuj1 nNOS	x	Tuj1, NeuN	Tuj1



**Figure 1. The organization and multiscale frame of the enteric nervous system**

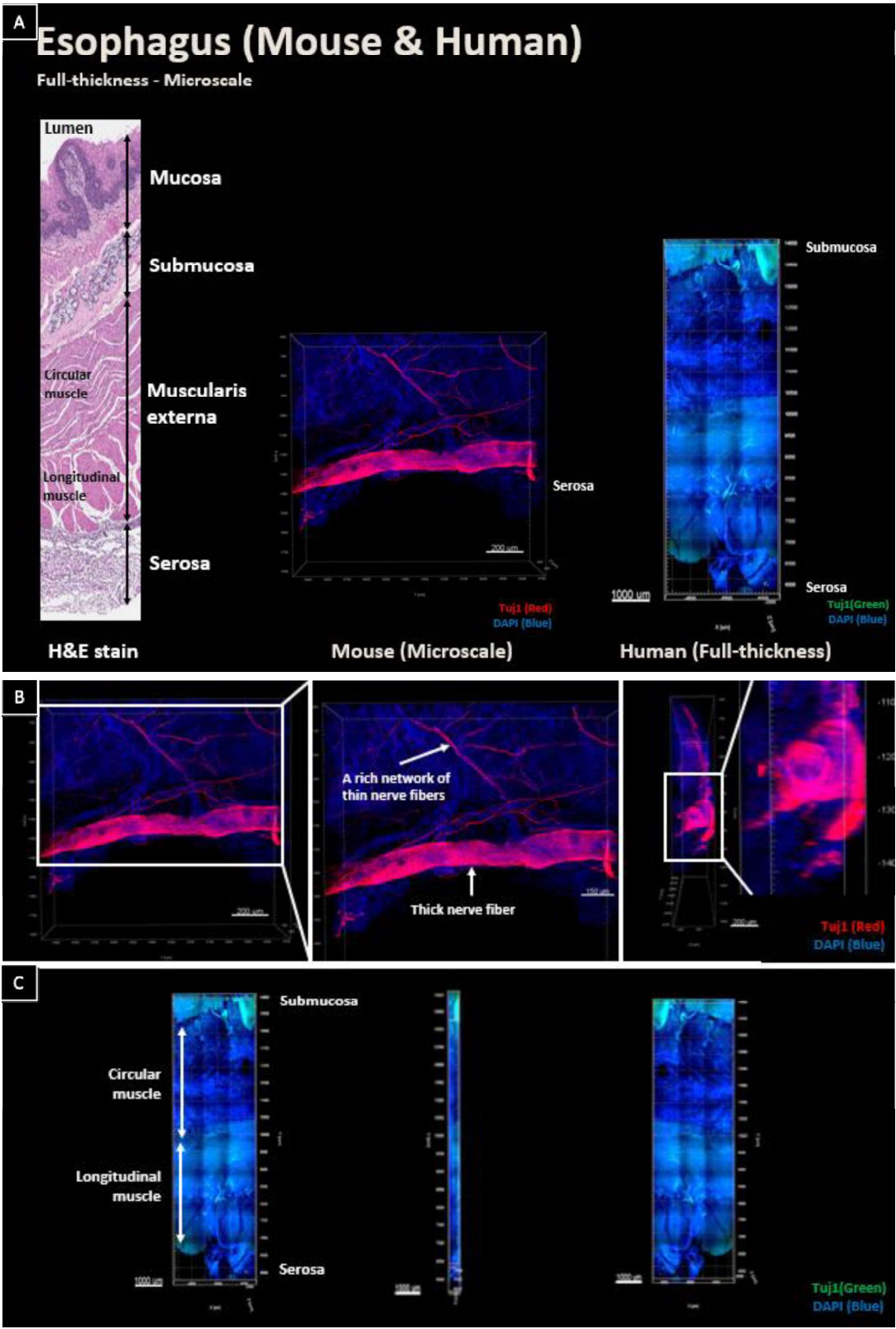
**(A)** Diagrammatic view of the arrangement of the ENS in the GI tract.

**(B)** A multiscale framework of ENS in mouse and human. The image in the upper left corner is the whole GI tract level, followed by the organ level, mesoscale, full-thickness from mucosa to serosa, and the layer level is microscale. The cleared tissues were imaged from a macroscopic viewpoint to a microscopic point of view.



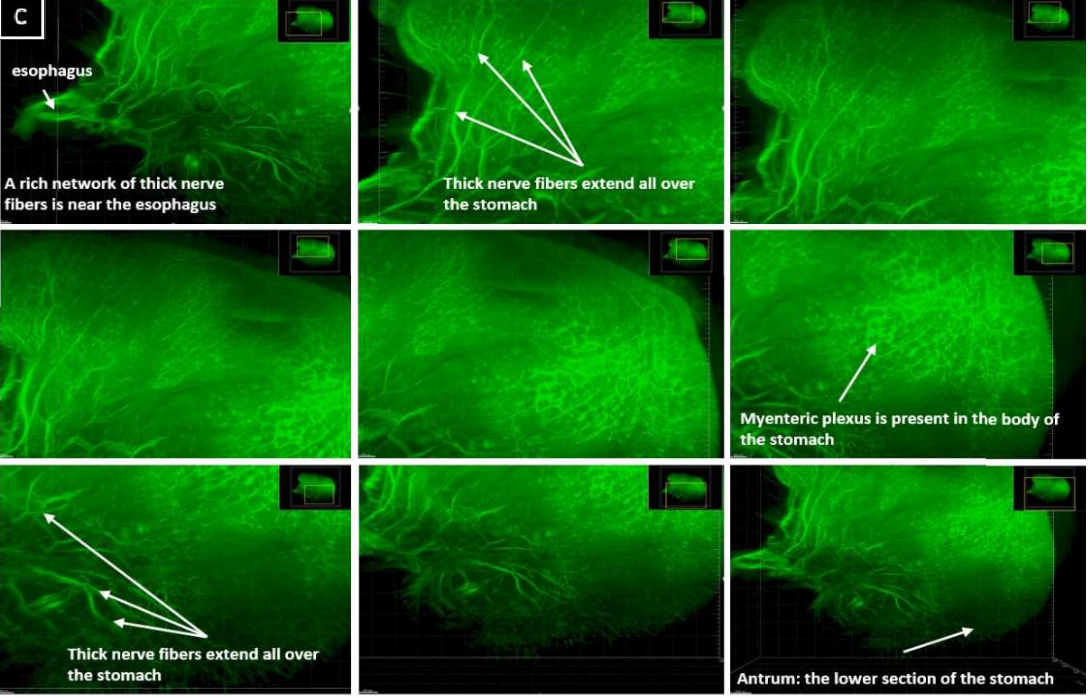
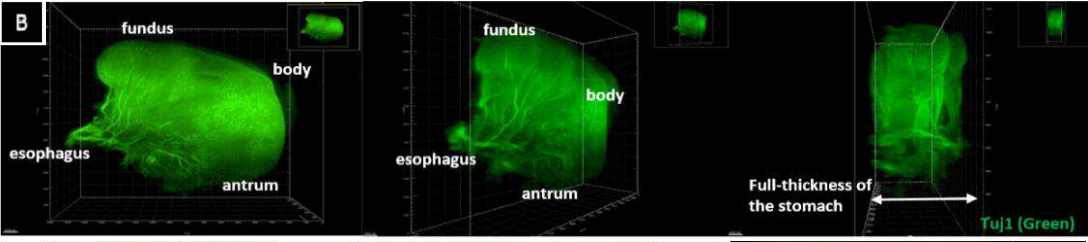
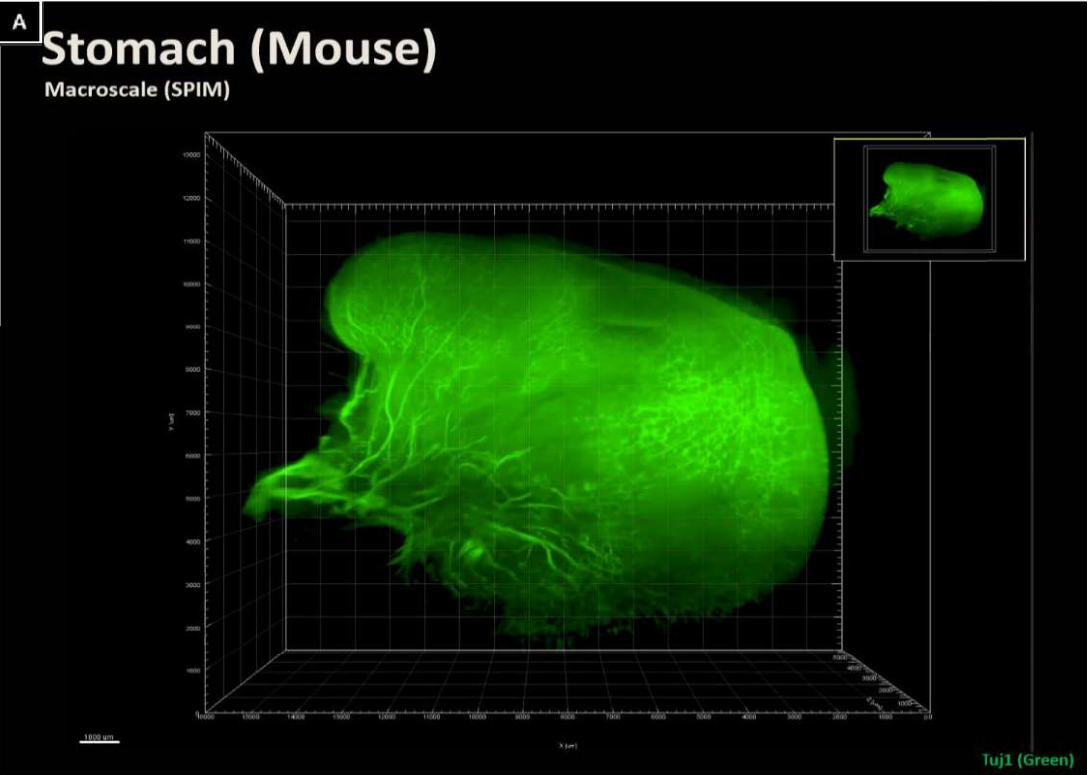
**Figure 2. Macroscale and mesoscale of esophagus ENS in mouse**

**(A)** 3D reconstruction of cleared ChAT-Cre tdTomato mouse esophagus (SPIM,  $16 \times 14 \times 5.3$  mm). Scale bar:  $300 \mu\text{m}$ . **(B)** Front side of view, right side of view, and back side view. Scale bar:  $500 \mu\text{m}$ . **(C)** The high-magnification images from the arrows. Each arrow indicates inner and outer muscle and location of cardiac parts in the stomach. Scale bar:  $800 \mu\text{m}$ .



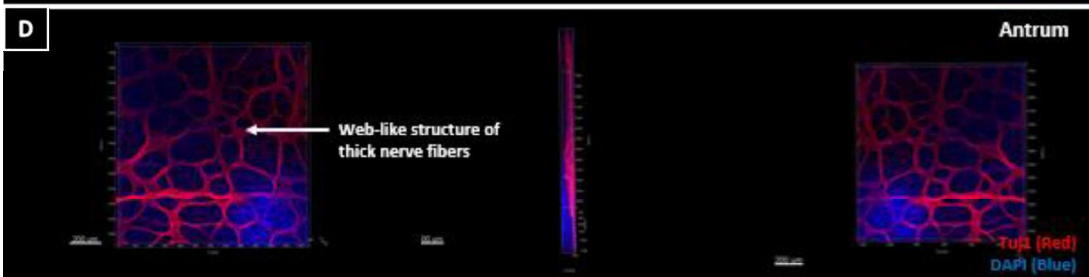
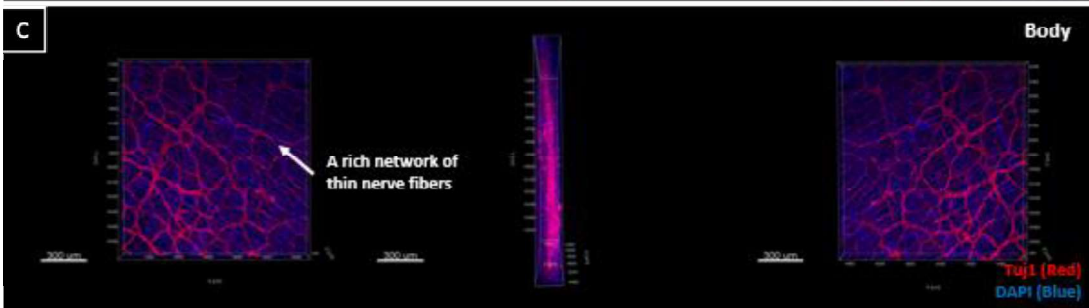
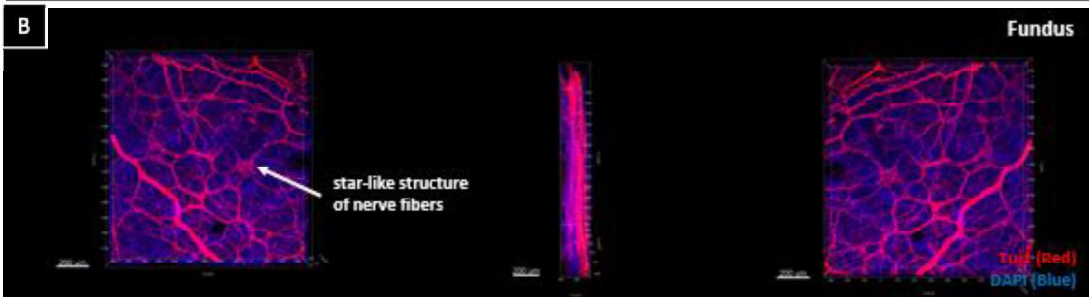
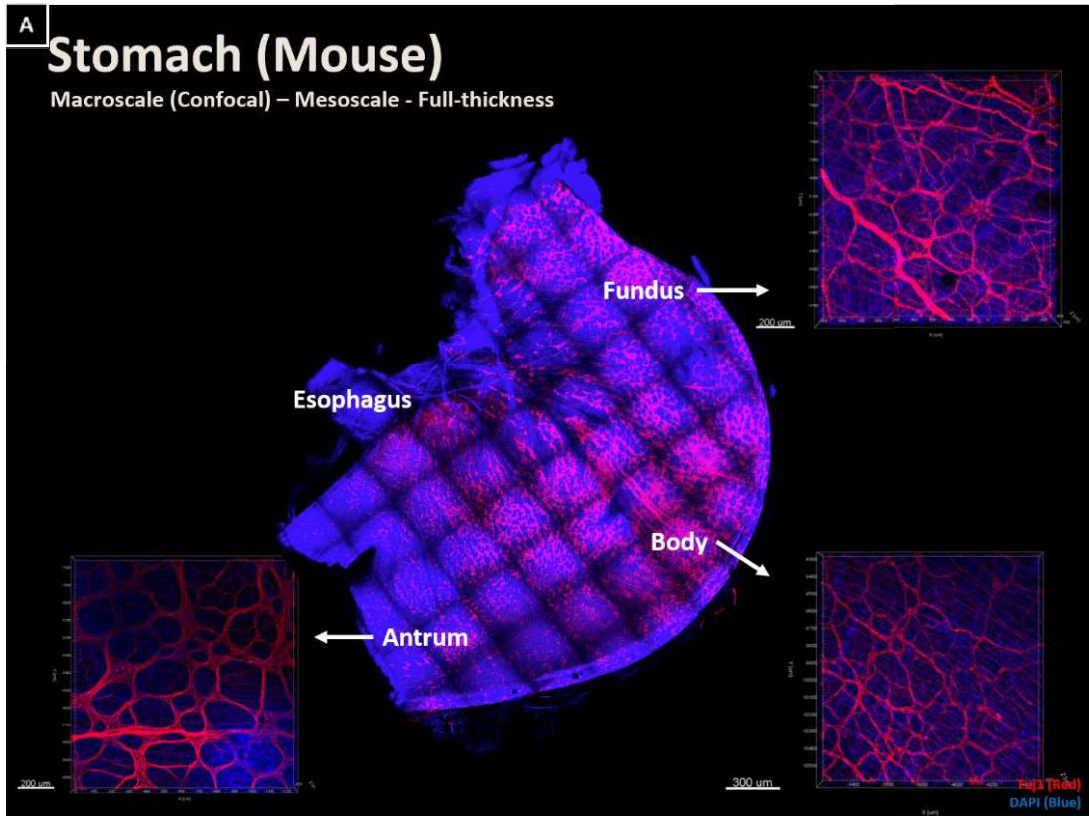
**Figure 3. Full-thickness and microscale of esophagus ENS in mouse and human**

(A) Comparison between the 3D ENS structure of mouse and human esophagus in two dimensions (H&E stain). (B) The white box indicates the area enlarged in just the right image. The microscale level of the mouse esophagus was imaged with Tuj1 (red) and DAPI (blue) antibodies (10× objective, stitched fields,  $1.26 \times 1.26 \times 0.23$  mm). Scale bar: 150–200  $\mu\text{m}$ . (C) Human esophagus from mucosa to submucosa stained with Tuj1 (green) and DAPI (blue) antibodies (10× objective, stitched fields,  $3.3 \times 8.38 \times 0.42$  mm). Front side of view, Right side of view, and Back side view. Scale bar: 500  $\mu\text{m}$ .



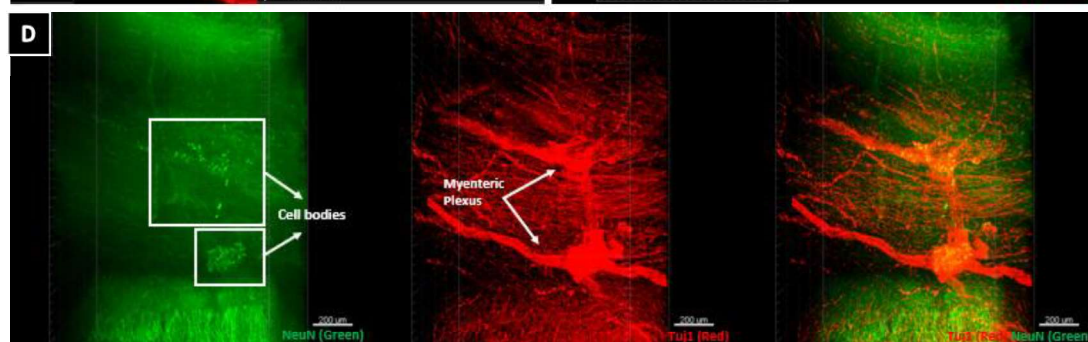
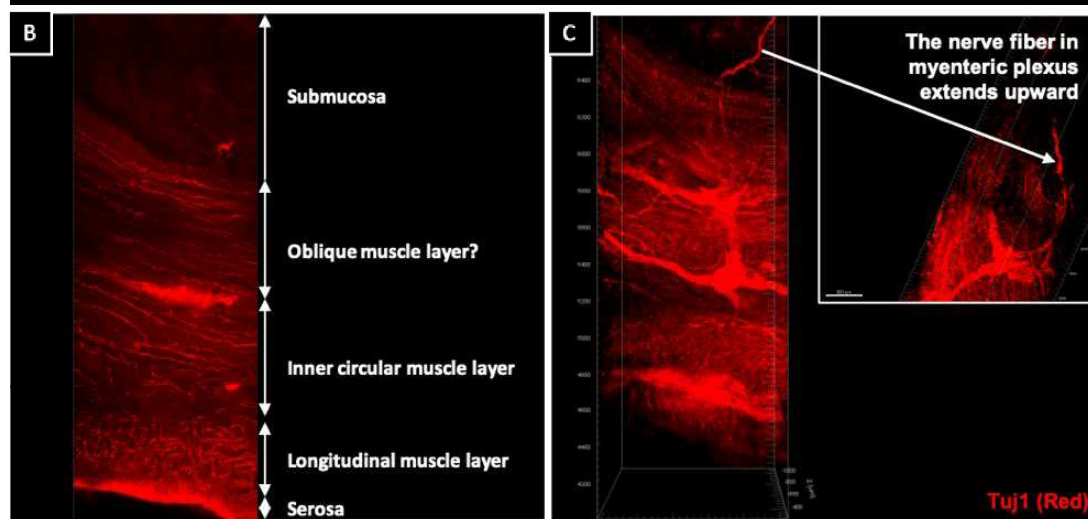
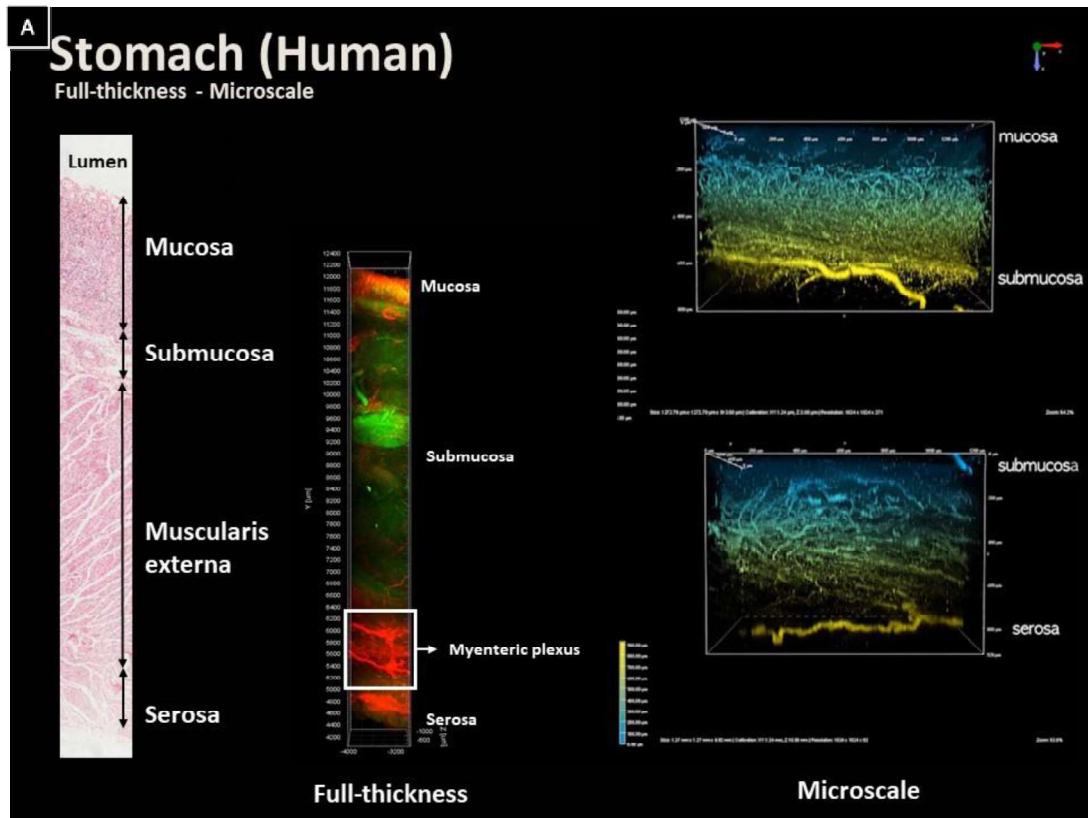
**Figure 4. Macroscale and mesoscale of stomach ENS in mouse**

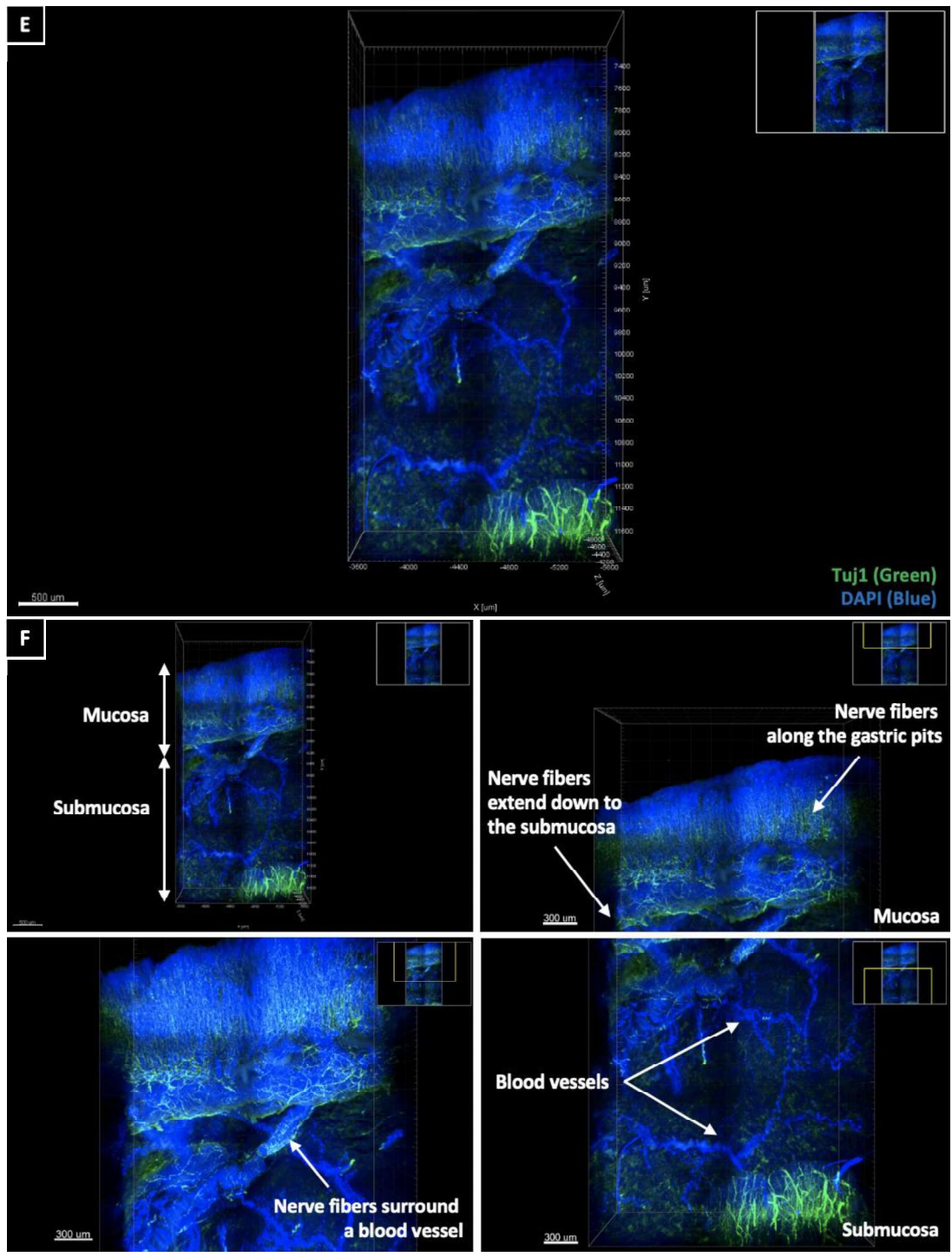
**(A)** The image of Tuj1 (green) positive neurons in the whole mouse stomach. (SPIM,  $16 \times 13 \times 5$  mm). **(B)** Front side of view, Right side of view, and Back side view. 3D ENS structure of mouse whole stomach. Scale bar:  $1000 \mu\text{m}$ . **(C)** Immunofluorescent SPIM images of the different stomach regions in the mouse. Representative SPIM images demonstrating a channel for Tuj1 present in the mouse whole stomach. **(B and C)** Scale bar:  $500 \mu\text{m}$ .



**Figure 5. Mesoscale and microscale of stomach ENS in mouse**

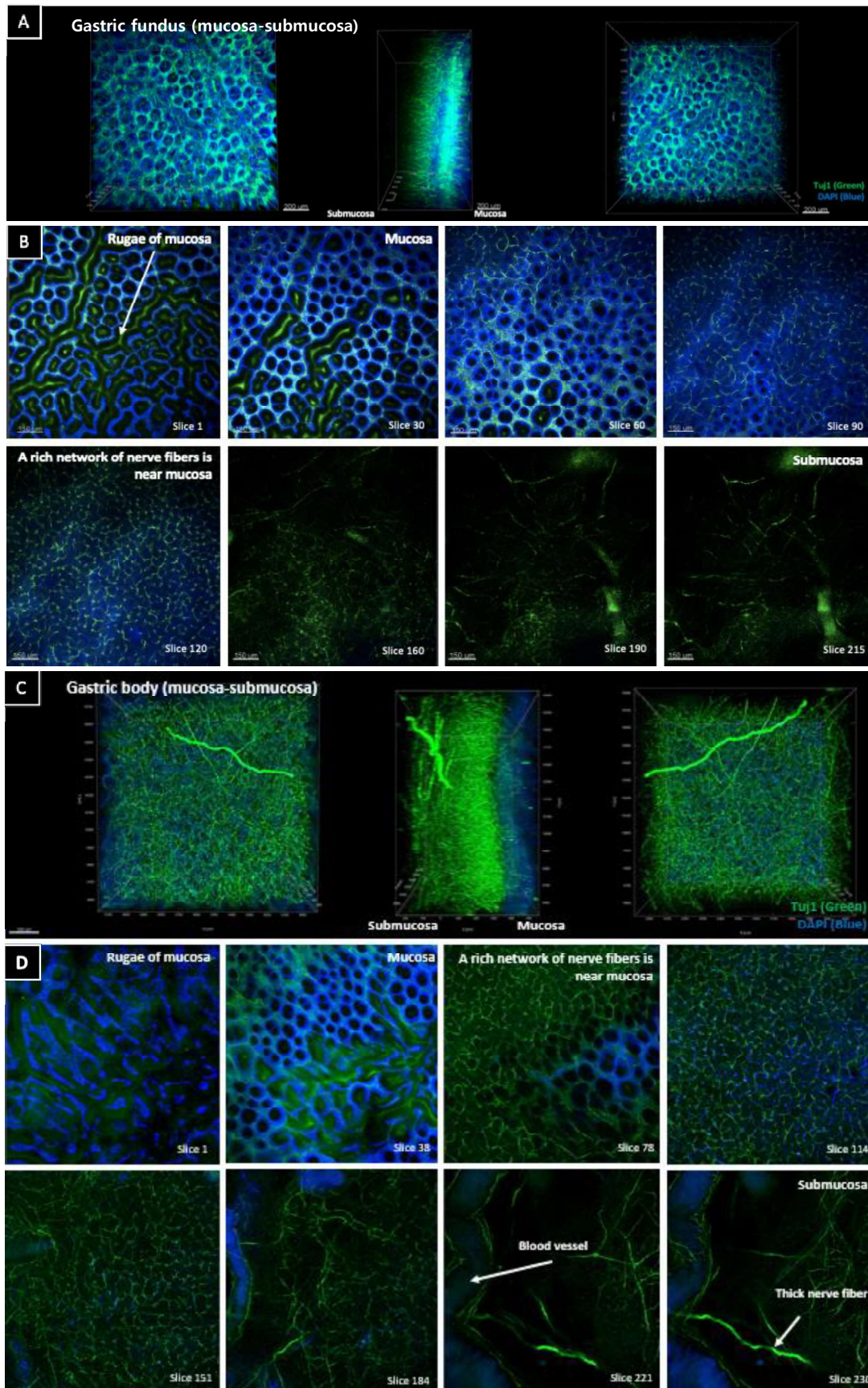
**(A)** Representative confocal images of mouse whole stomach ( $10\times$  objective, stitched fields,  $12.6 \times 12.6$  mm). Microscale images show the stomach of wild-type mouse stained for Tuj1 (red). **(B)** Confocal Z-stack fundus region image of the stomach ( $10\times$  objective,  $1.24 \times 1.3 \times 0.18$  mm). Scale bar:  $200 \mu\text{m}$  **(C)** Confocal Z-stack body region image of the stomach ( $10\times$  objective,  $1.24 \times 1.3 \times 0.14$  mm). Scale bar:  $300 \mu\text{m}$  **(D)** Confocal Z-stack antrum region image of the stomach ( $10\times$  objective,  $1.24 \times 1.3 \times 0.084$  mm). Scale bar:  $200 \mu\text{m}$  **(B–D)** Front side of view, Right side of view, and Back side view.





**Figure 6. Full-thickness and microscale of stomach ENS in human**

**(A)** Comparison between the 3D ENS structure of human stomach and two dimensions (H&E stain). Full-thickness confocal image of human fundus stained with Tuj1 (red) and NeuN (green) antibodies (10× objective, stitched fields, 1.06 × 8.38 × 0.84 mm). Scale bar: 1000 μm. Microscale of the stomach from mucosa to serosa and submucosa to serosa (depth-dependent color-code). **(B)** Histology of human stomach ENS structure. **(C)** An arrow represents that the nerve fiber in myenteric plexus extends upward. **(D)** Double-labeled image of myenteric plexus decomposed into individual fluorophores. Small clustered ganglia have NeuN (green), Tuj1 (red) imaged with 10× objective. Tuj1 neuron fibers include all cell bodies within myenteric ganglia. **(B–D)** Scale bar: 200 μm. **(E)** Human antrum of the stomach approximately 4 mm from mucosa to submucosa and stained with Tuj1 (green) and DAPI (blue) antibodies (10× objective, 2.19 × 4.38 × 0.81 mm). Scale bar: 500 μm. **(F)** Nerve fibers extend down to the submucosa and follow along with the gastric pits. There are blood vessels in the space between mucosa and submucosa. Scale bar: 300 μm.



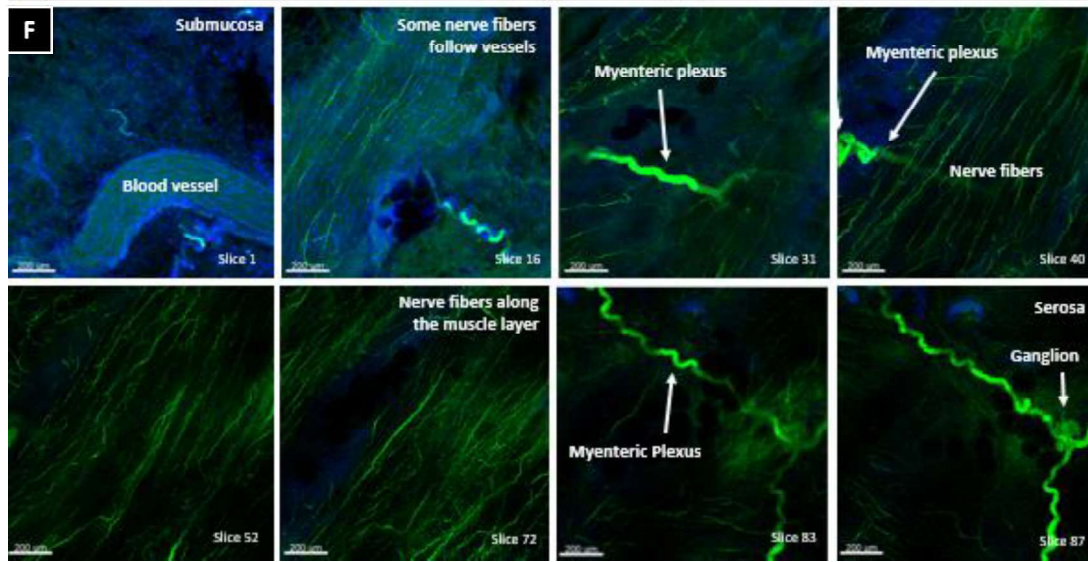
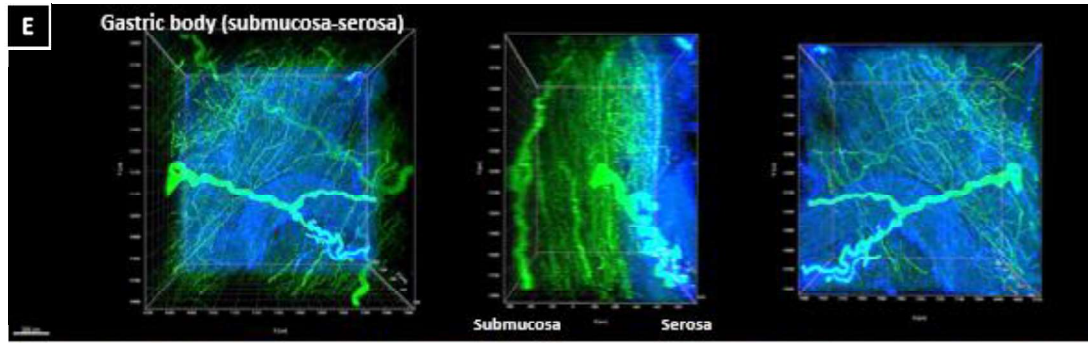


**Figure 7. Microscale of stomach ENS in human**

**(A)** Mucosa region of the fundus stained with Tuj1 (green) and DAPI (blue) ( $10\times$  objective,  $1.23 \times 1.3 \times 0.64$  mm). Scale bar:  $200 \mu\text{m}$ . **(B)** Lower numbers are closer to rugae of mucosa. Scale bar:  $150 \mu\text{m}$ . **(C)** The body of the stomach approximately  $0.813$  mm from mucosa to submucosa and stained with Tuj1 (green) and DAPI (blue) antibodies. ( $10\times$  objective,  $1.24 \times 1.3 \times 0.81$  mm). **(D)** Lower numbers are closer to the rugae of the mucosa, and higher numbers are closer to the submucosa. **(E)** Three-dimensional ENS structure of the body of the stomach from submucosa to serosa ( $10\times$  objective,  $1.24 \times 1.3 \times 0.92$  mm). **(A, C, and E)** Front side of view, Right side of view, and Back side view. **(B, D and F)** Identified single slices from Z-stack in transition zone. **(F)** Lower numbers are closer to the submucosa, and higher numbers are closer to serosa. **(C–F)** Scale bar:  $200 \mu\text{m}$ .

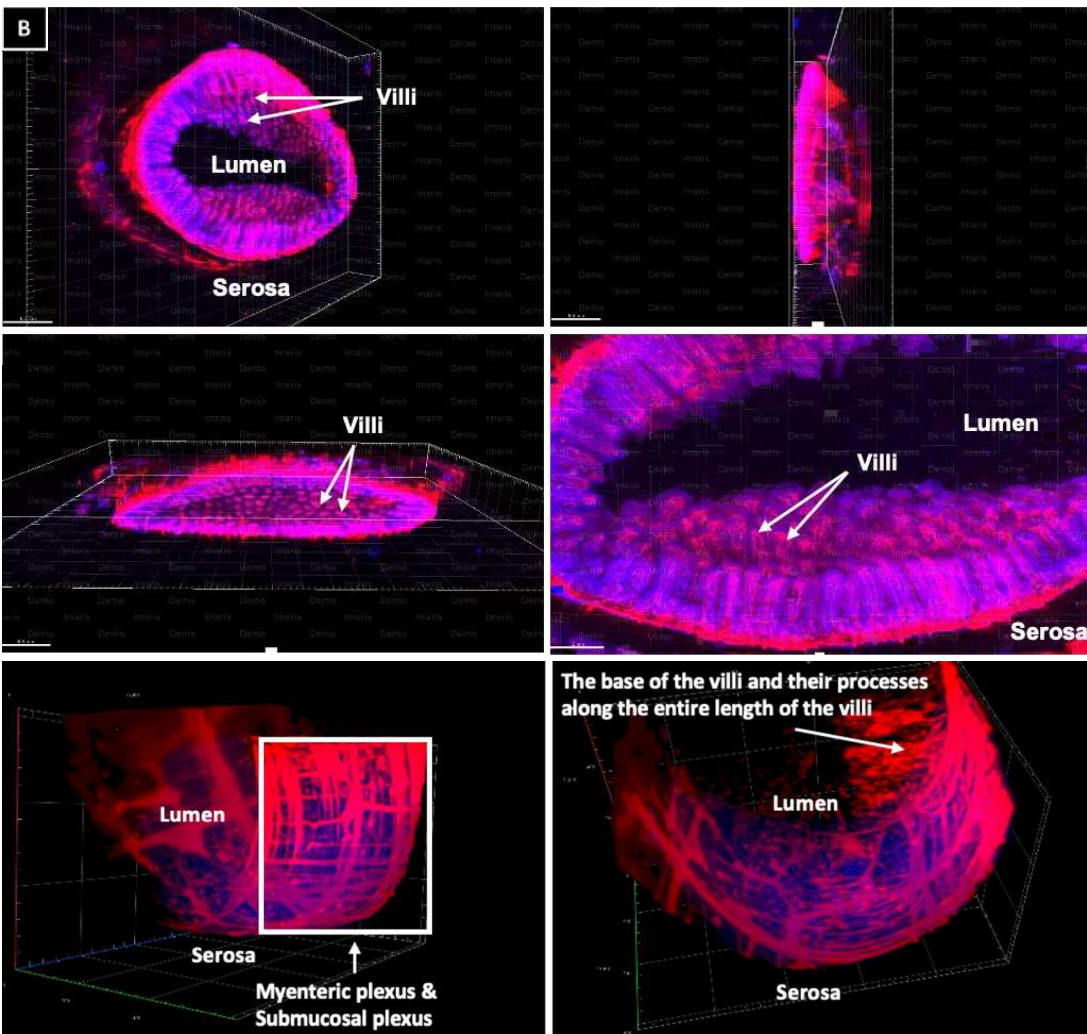
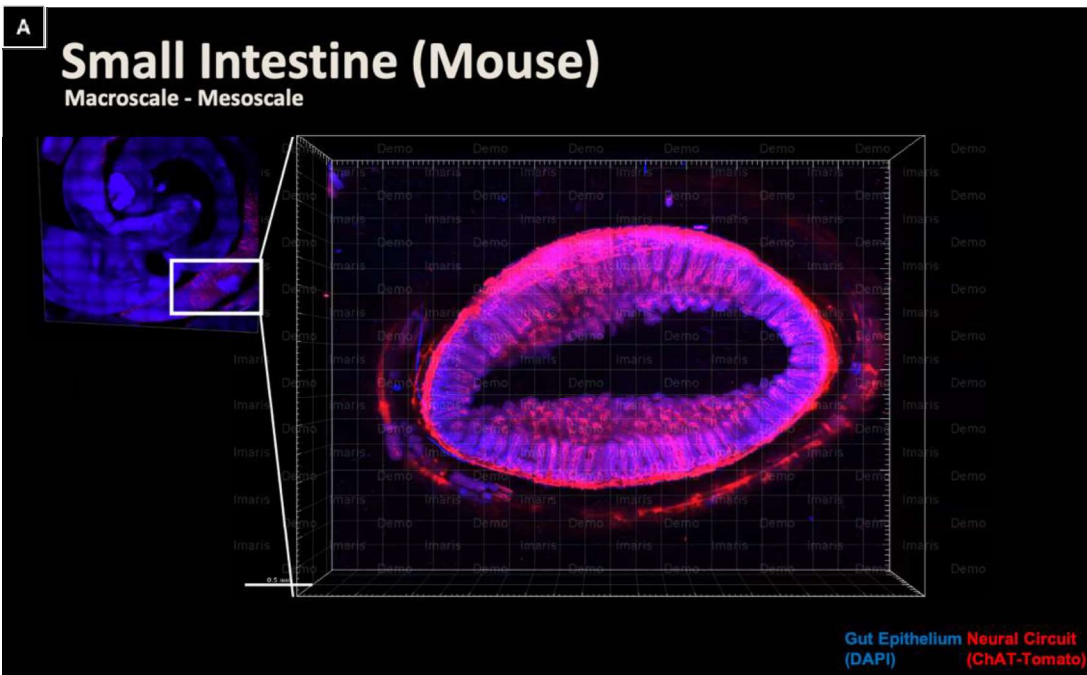


**Figure 8. Macroscale and mesoscale of small intestine ENS in mouse**

**(A)** The white box shows the mesoscale level of the small intestine in macroscale, and the right side is an enlarged image (Leica,  $4.7 \times 3.5 \times 3$  mm). **(B)** Each image represents ENS structures in the small intestine. Inner cavity of the small intestine is the lumen, and the serosa is outermost layer of the intestine. Intestinal villi are small, finger-like projections that extend into the lumen. The submucosal and myenteric plexus lies in the intestinal wall. **(A and B)** Scale bar:  $500 \mu\text{m}$ .

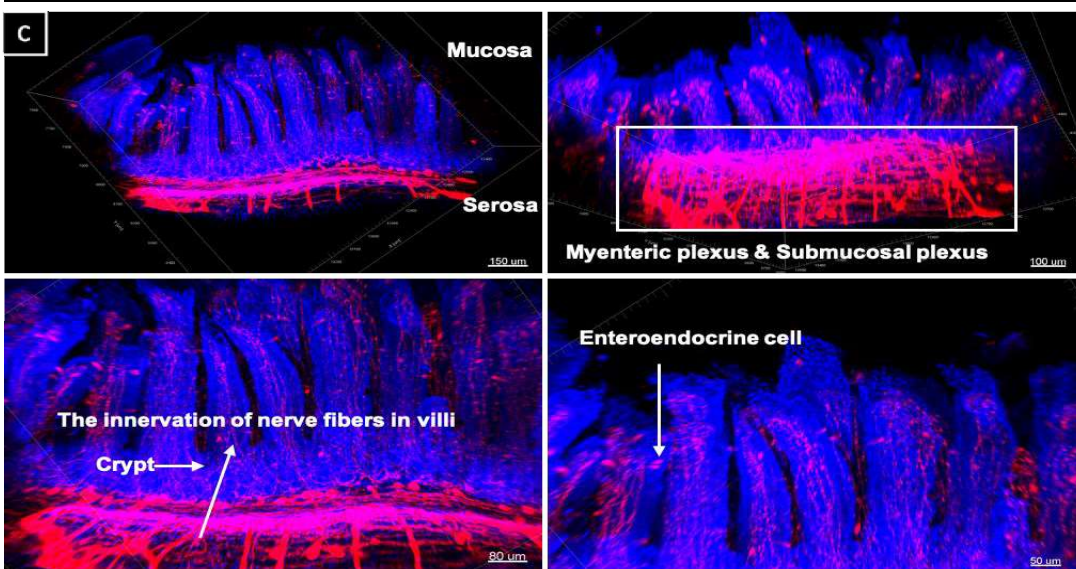
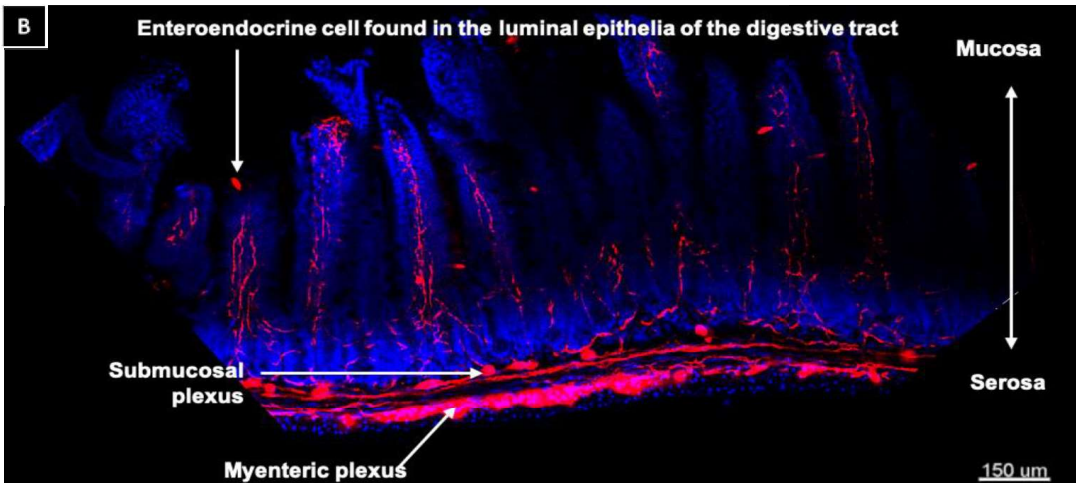
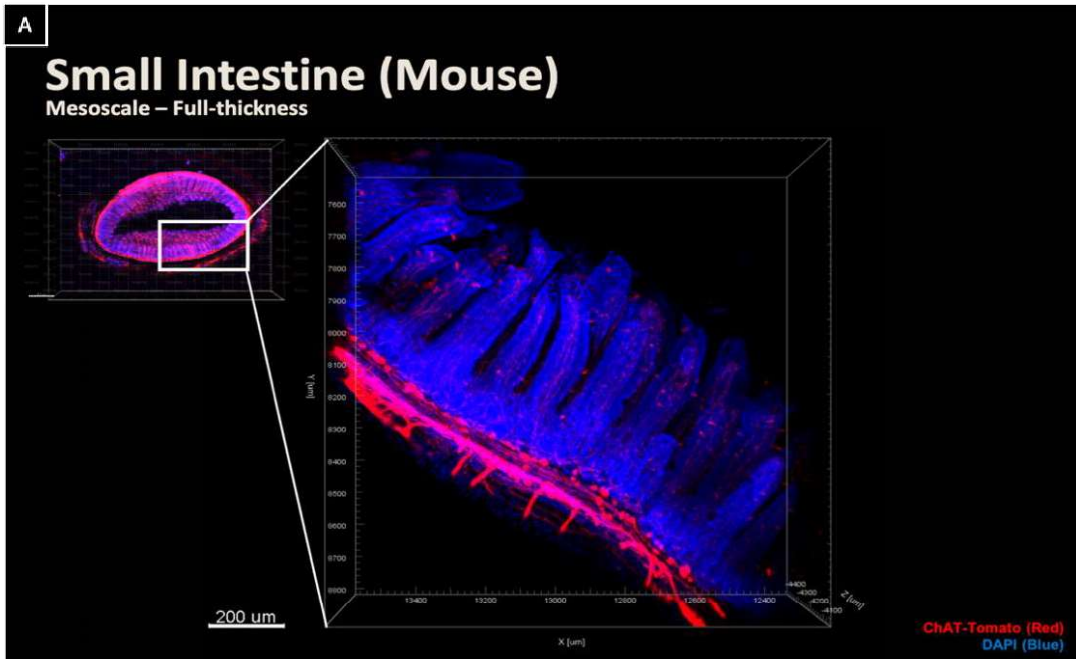


**Figure 9. Mesoscale and full thickness of small intestine ENS in mouse**

**(A)** The white box shows the full thickness of the mouse small intestine in the mesoscale, and the right side is an enlarged image (10× objective, 12 × 13 × 3.5 mm). Scale bar: 200  $\mu\text{m}$ . **(B)** Full thickness of small intestinal tissue from mucosa to serosa. Each arrow represents the ENS structure in the small intestine. Scale bar: 150  $\mu\text{m}$ . **(C)** Each arrow indicates ENS structures. Scale bar: top left 150  $\mu\text{m}$ , top right: 100  $\mu\text{m}$ , bottom left: 80  $\mu\text{m}$ , bottom right: 50  $\mu\text{m}$ .

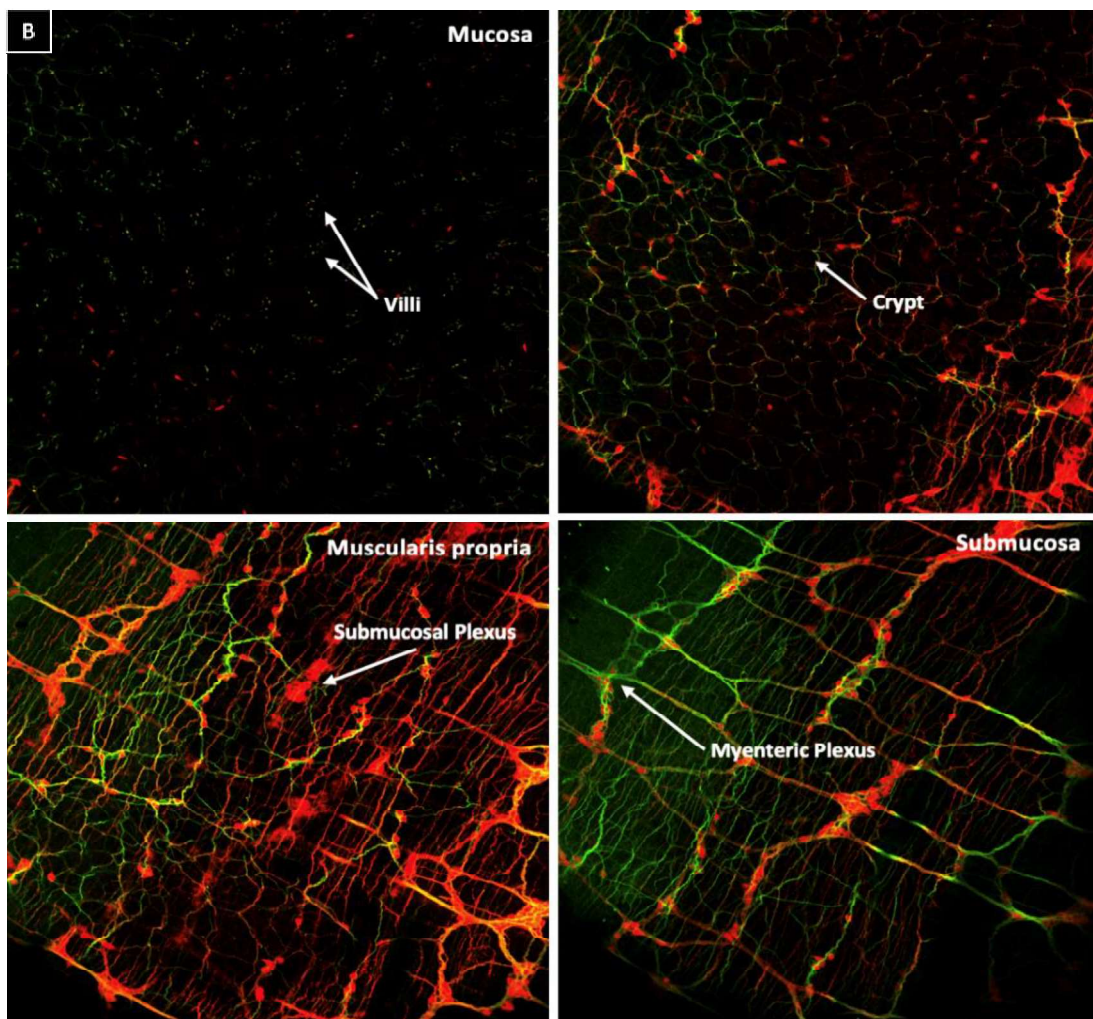
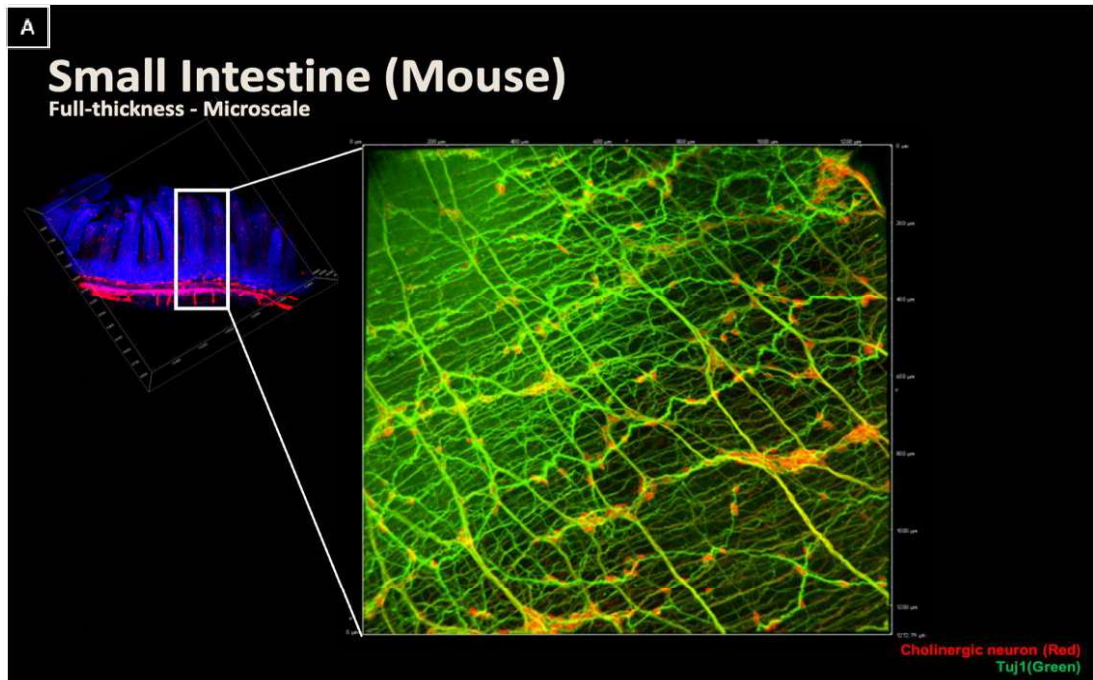


**Figure 10. Full-thickness and microscale of small intestine ENS in mouse**

**(A)** The white box shows the microscale of the mouse small intestine in the full-thickness, and the right side is an enlarged image ( $10\times$  objective,  $1.2 \times 1.3 \times 0.84$  mm). Scale bar:  $200 \mu\text{m}$ . **(B)** Identified single slices from Z-stacks in transition zone. Scale bar:  $150 \mu\text{m}$ .

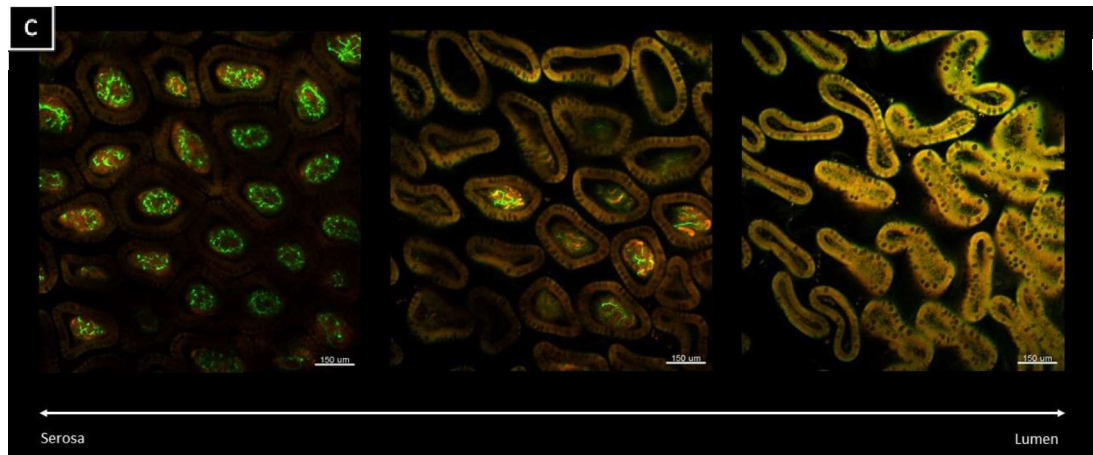
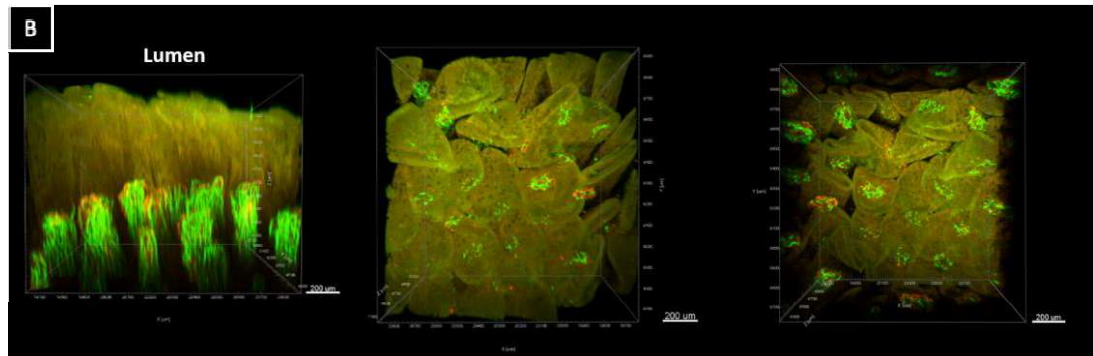
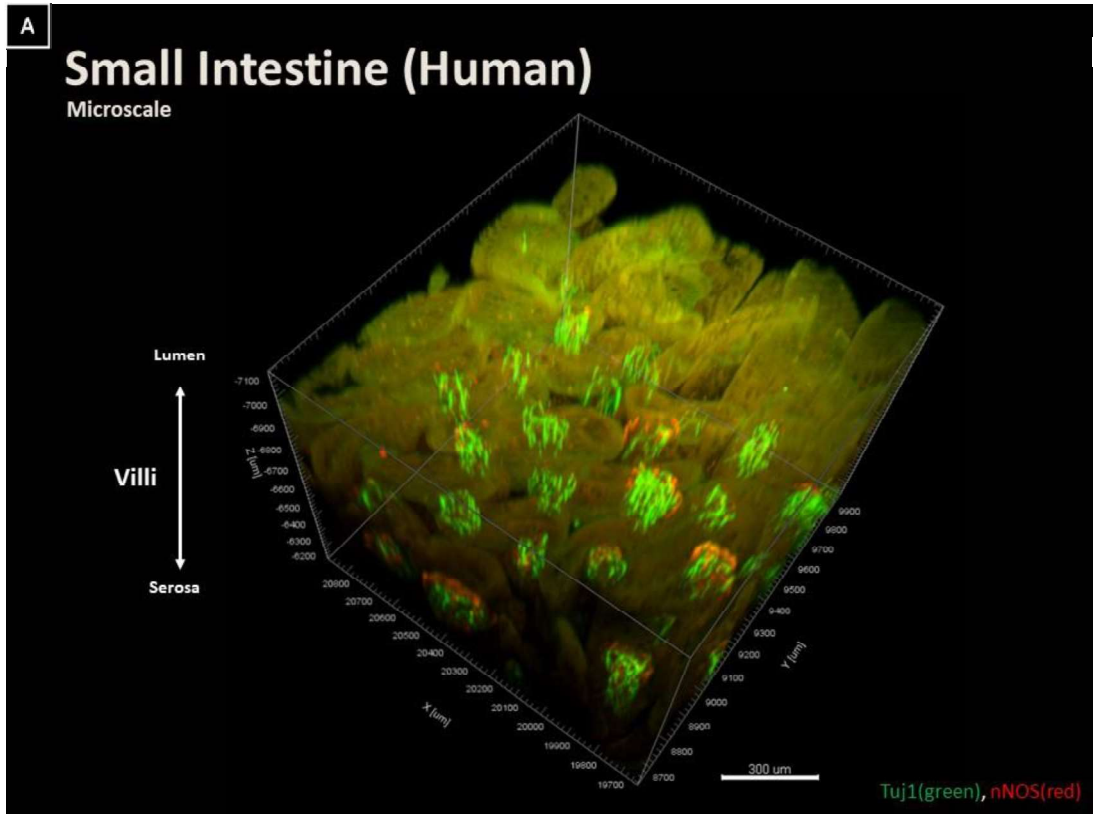


**Figure 11. Microscale of small intestine ENS in human**

**(A)** Villi of the mucosa region stained with Tuj1 (green) and nNOS (red) ( $10\times$  objective,  $1 \times 1.3 \times 0.98$  mm). Scale bar:  $300 \mu\text{m}$ . **(B)** Each image represents ENS structures of villi in the small intestine. Scale bar:  $200 \mu\text{m}$ . **(C)** Representative horizontal cross-sectional view of confocal microscopic images showing villi of the small intestine. Scale bar:  $150 \mu\text{m}$ .

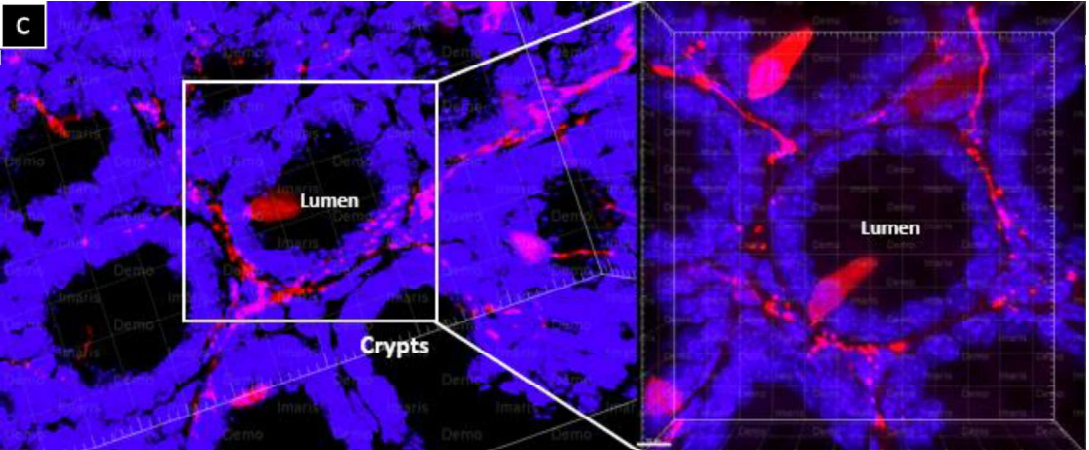
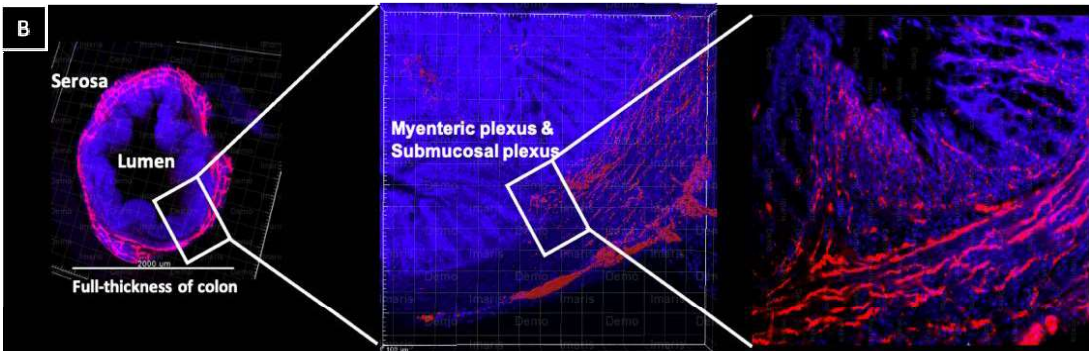
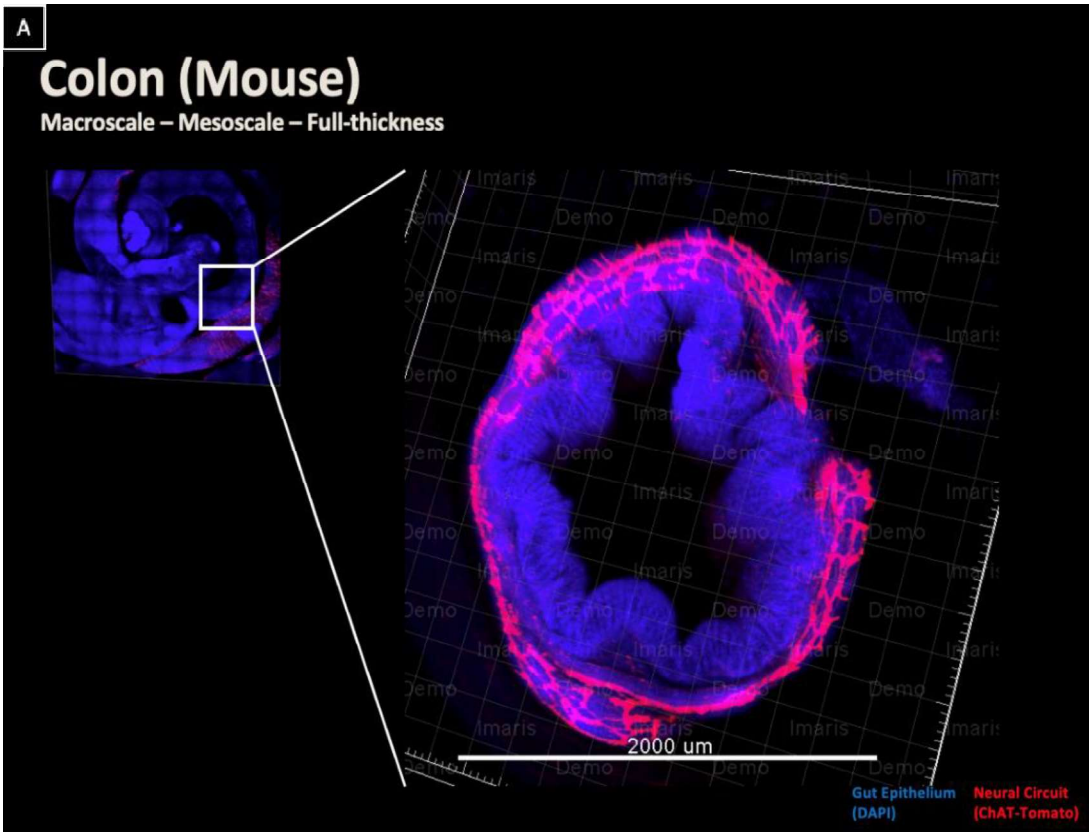


**Figure 12. Macroscale and mesoscale of colon ENS in mouse**

**(A)** The white box shows the mesoscale of the mouse colon in the macroscale, and the right side is an enlarged image ( $10\times$  objective,  $2.5 \times 2.5 \times 0.5$  mm). Scale bar:  $2000 \mu\text{m}$ . **(B)** Inner cavity of the colon is the lumen, and the serosa is outermost layer of the intestine. **(C)** 3D visualization of the intestinal crypts in the mouse. Lower numbers are closer to serosa, and higher numbers are closer to the mucosa.

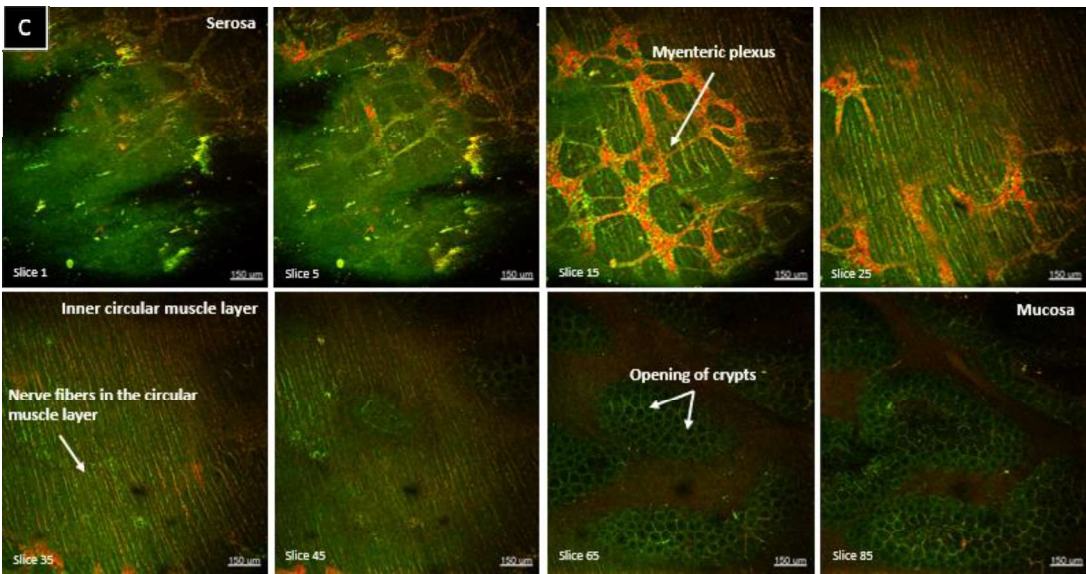
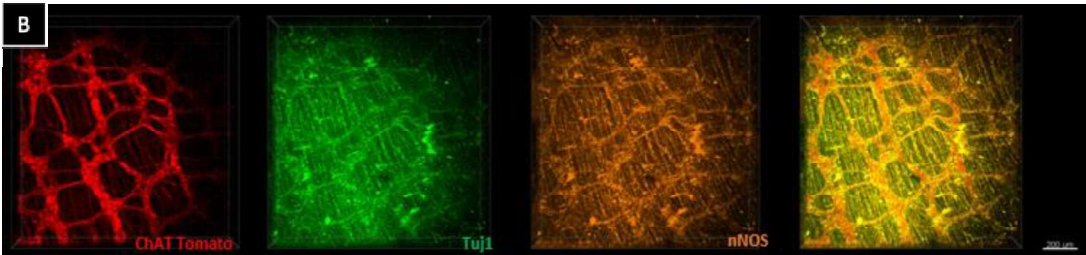
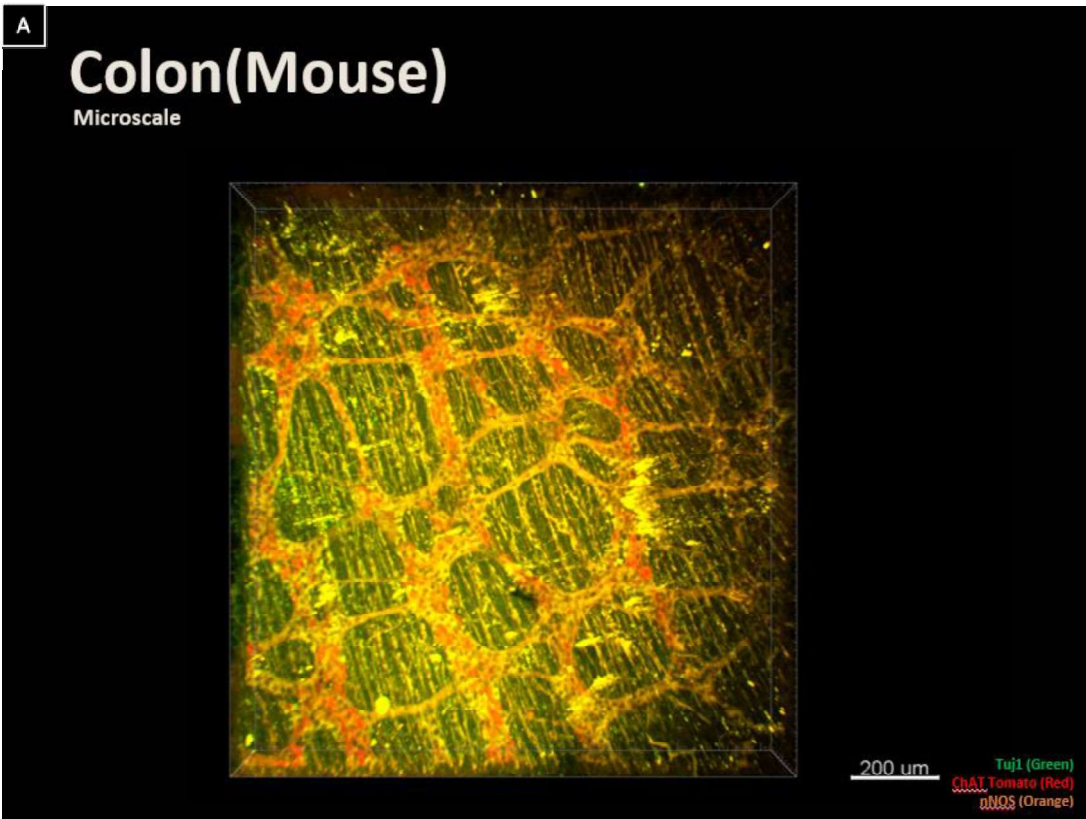


**Figure 13. Microscale of colon ENS in mouse**

(A) Microscale of mouse colon stained with Tuj1 (green) and nNOS (orange) antibodies (10× objective, 1.2 × 1.2 × 0.17 mm). (B) Human colon visualized with two antibodies, Tuj1 and nNOS. (A and B) Scale bar: 200 μm. (C) Snapshots of z-stack layer of the colon of ChAT-Cre tdTomato mouse. Identified single slices from Z-stacks in transition zone. Higher numbers are closer to mucosa. Scale bar: 150 μm.

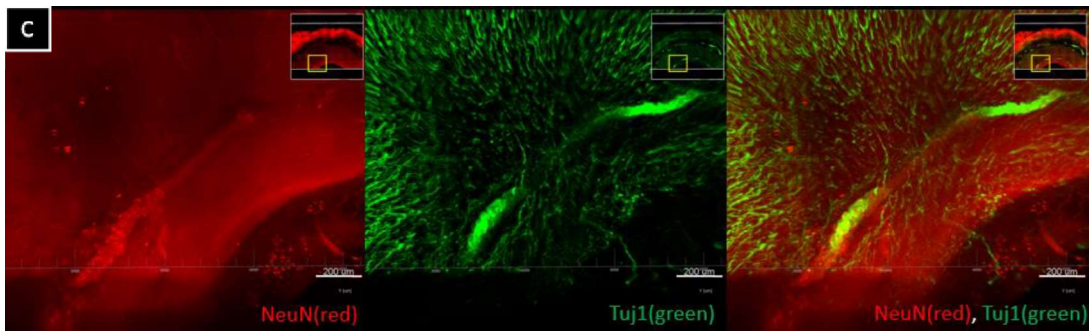
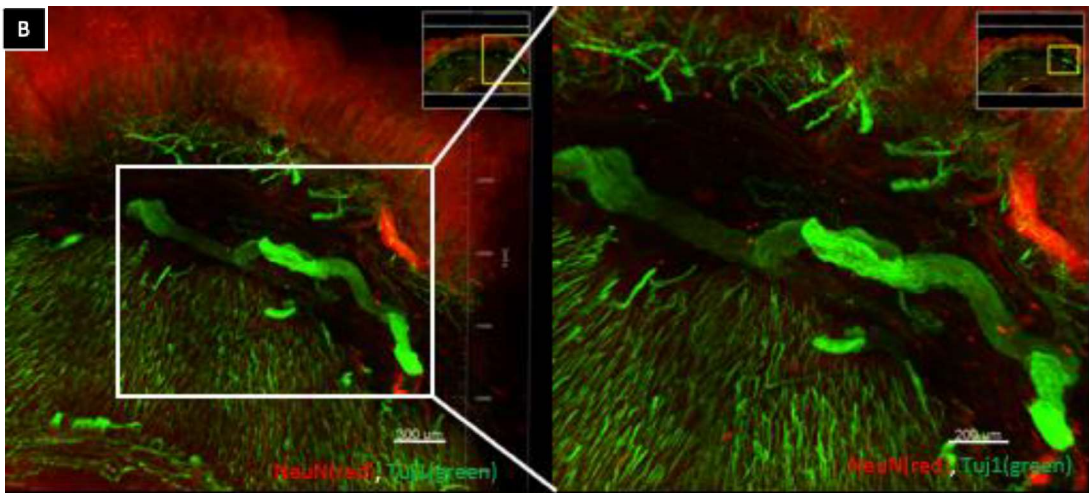
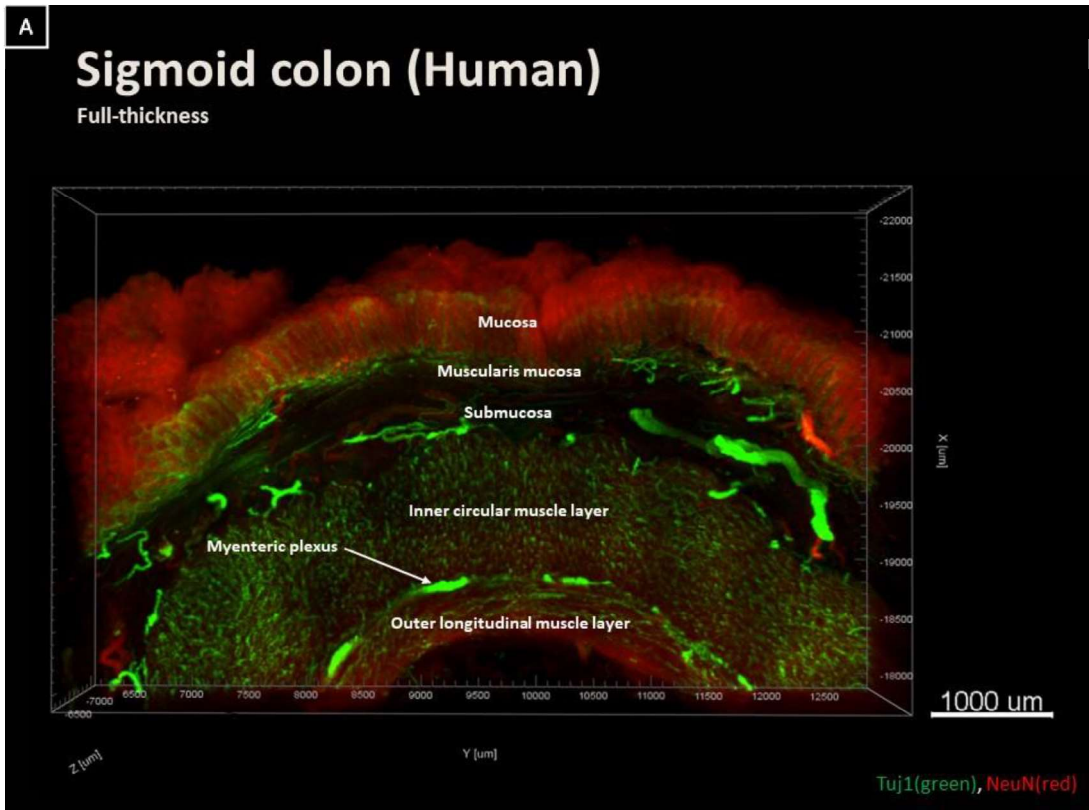


**Figure 14. Full-thickness of sigmoid colon ENS in a patient with Crohn's disease**

(A) Full-thickness confocal image of human sigmoid colon stained with Tuj1 (red) and NeuN (green) antibodies (10× objective, stitched fields, 5 × 8 × 0.98 mm). Scale bar: 1000  $\mu\text{m}$ . The gastrointestinal wall has general organization of GI tract. (B) Representative IHC images of the submucosal plexus in human sigmoid colon. Scale bar: 200–300  $\mu\text{m}$ . (C) Double-labeled image of myenteric plexus decomposed into individual fluorophores. Small clustered ganglia have NeuN (red) and Tuj1 (green) imaged with 10× objective. Tuj1 neuron fibers include all cell bodies within myenteric ganglia. Scale bar: 200  $\mu\text{m}$ .

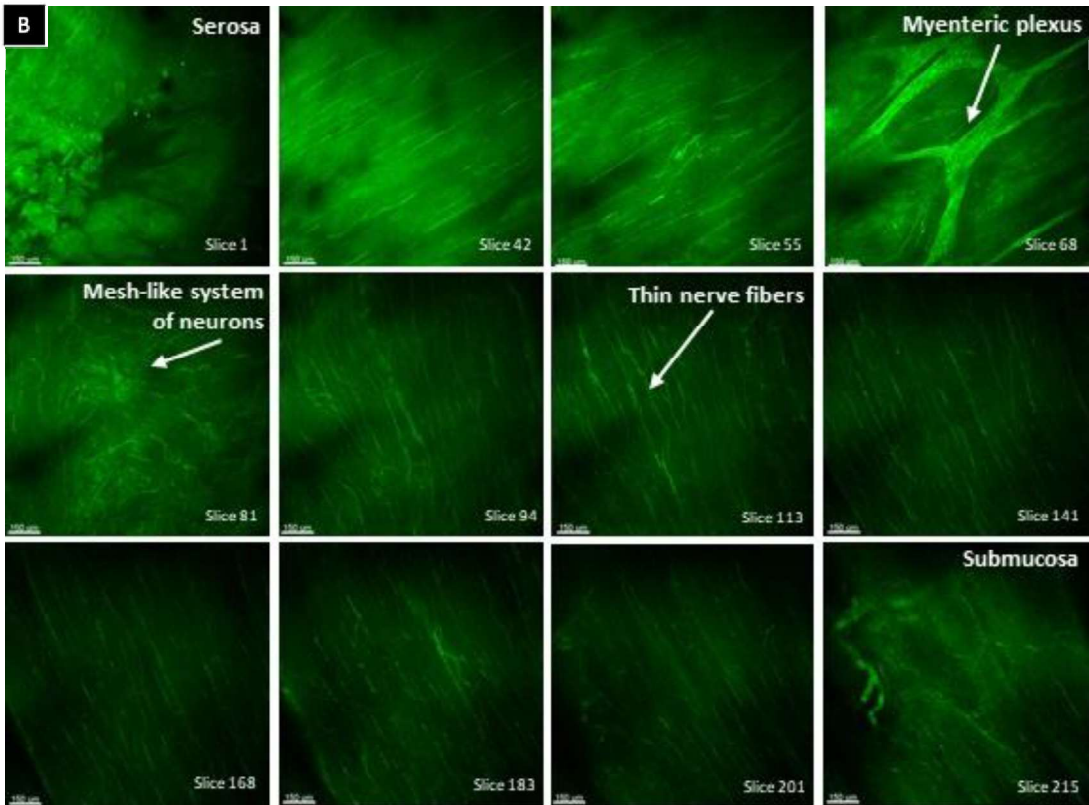
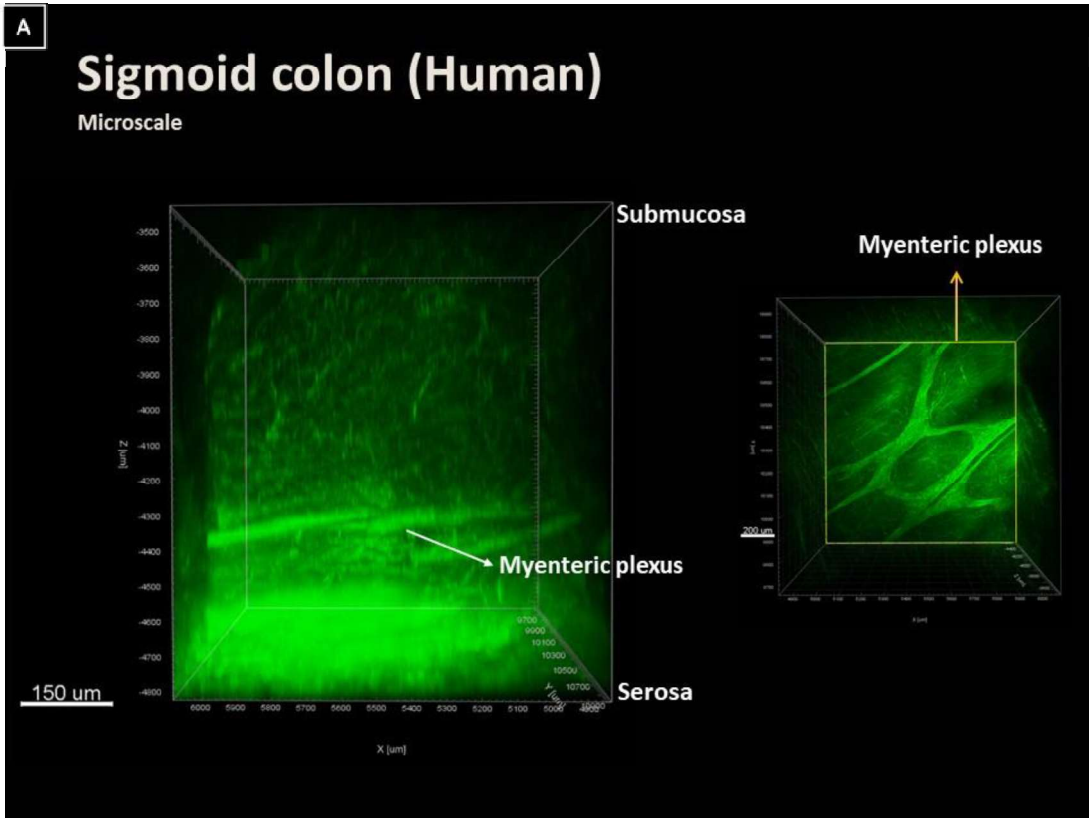


**Figure 15. Microscale of sigmoid colon ENS in human**

**(A)** Microscale human sigmoid colon from submucosa to serosa was imaged and stained with Tuj1 (green) and DAPI (blue) antibodies (10× objective, 1.2 × 1.3 × 1.4 mm). Scale bar: 500  $\mu\text{m}$ . **(B)** Lower numbers are closer to the serosa, and higher numbers are closer to the submucosa. Scale bar: 150  $\mu\text{m}$ .

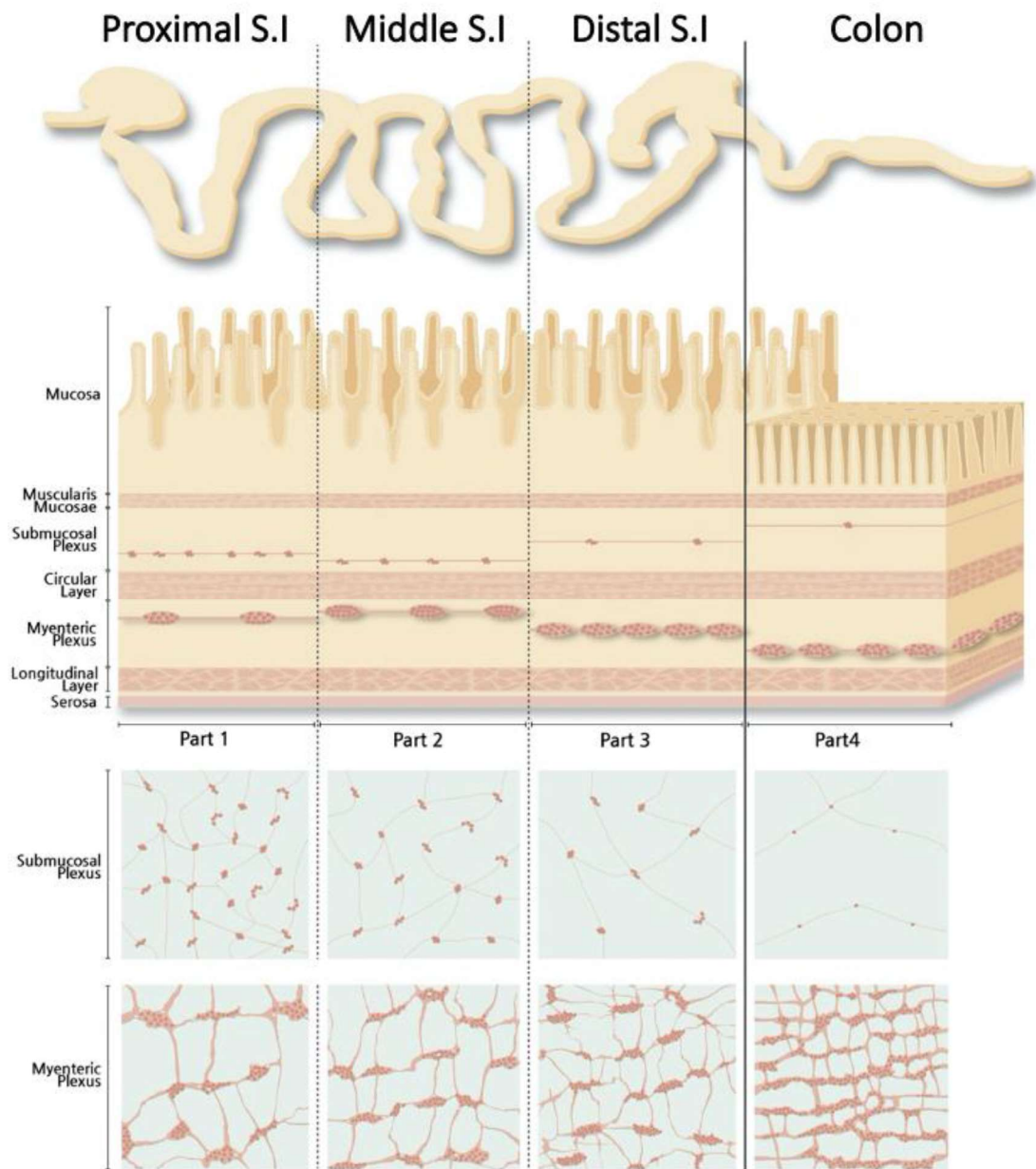


**Figure 16. Histology illustration of small intestine and colon in ChAT reporter mouse**

Whole fixed small intestine and colon were divided into four parts. Furthermore, proximal, middle, and distal small intestine were divided into four parts each, and the colon was divided into three parts: proximal, middle, and distal. It shows the distance-related morphological changes in the submucosal and myenteric plexus along the small intestine and colon of the mouse.

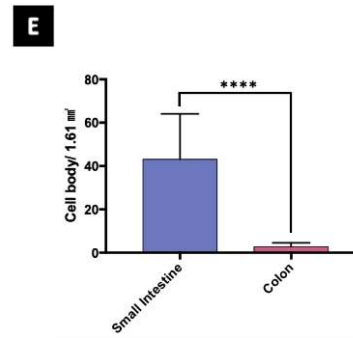
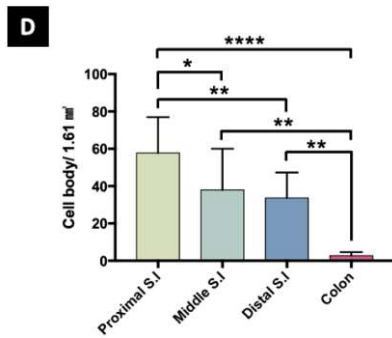
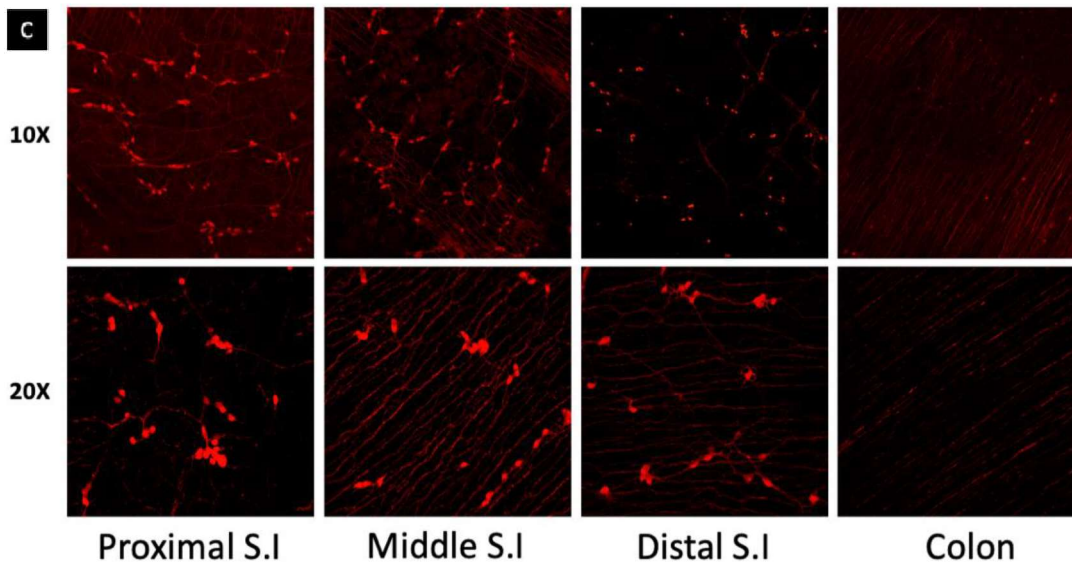
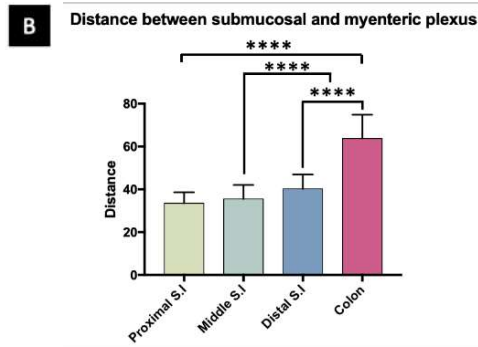
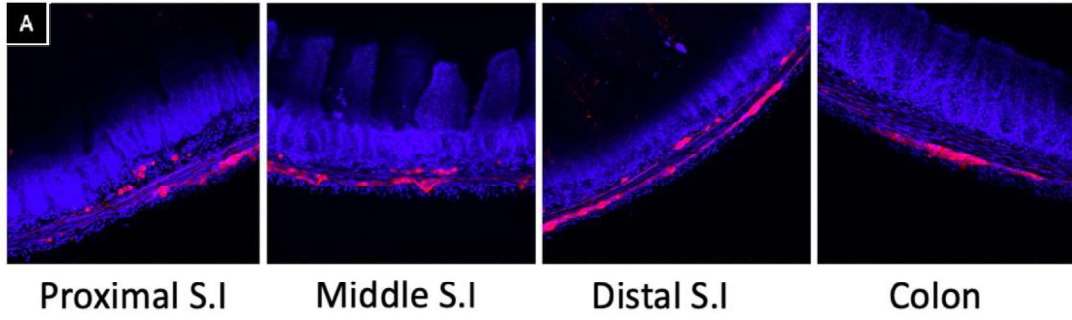


**Figure 17. Distance between two major plexus and quantification of cholinergic neurons in submucosal plexus**

**(A)** Four intestinal sample images represented as yz axis images illustrating the degree of full thickness from proximal small intestine to colon. **(B)** Distance between the submucosal and myenteric plexus ( $****P < 0.0001$ ). **(C)** The upper panels are  $10\times$  magnification and the lower panels are  $20\times$  magnification. **(D)** Quantification of neuronal cell bodies in submucosal plexus ( $*P = 0.0170$ ;  $**P = 0.0002$ ; and  $****P < 0.0001$ ). **(E)** Comparison of the number of cell bodies in submucosal plexus between small intestine and colon ( $****P < 0.0001$ ).

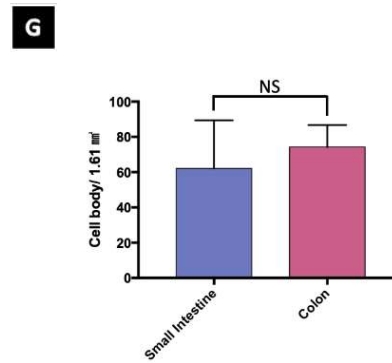
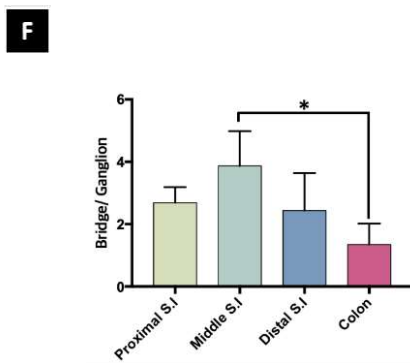
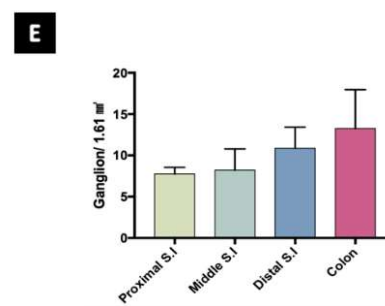
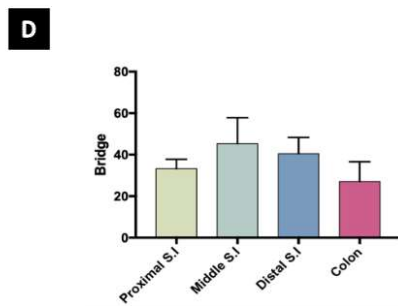
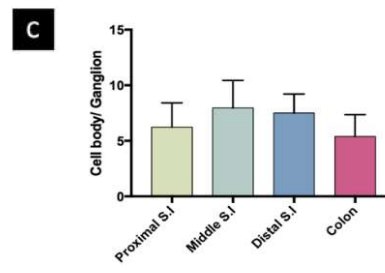
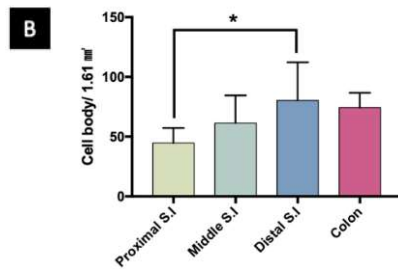
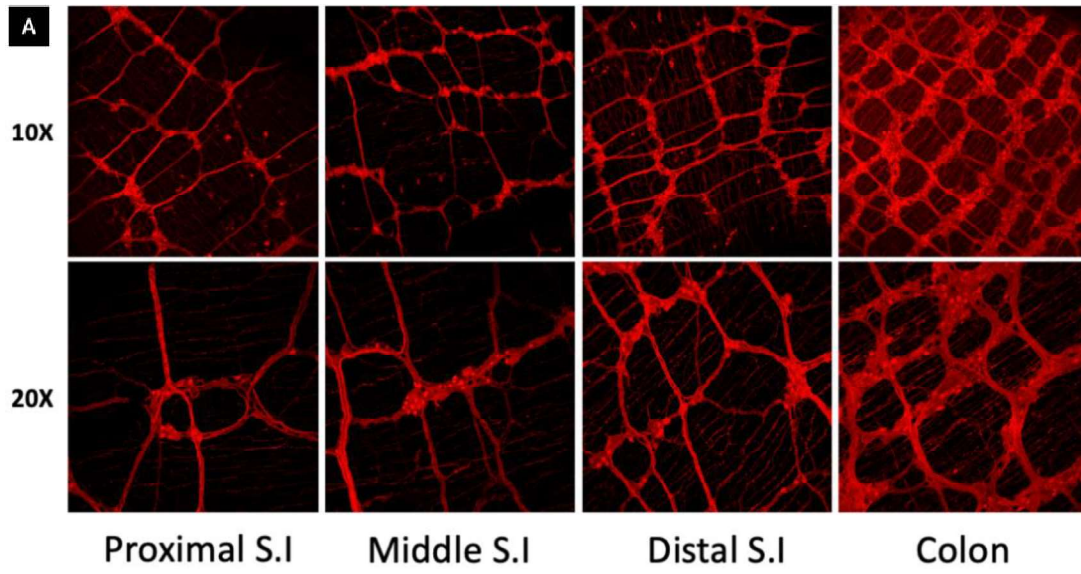


**Figure 18. Quantification of cholinergic neurons in myenteric plexus**

(A) The upper panels are 10× magnification and the lower panels are 20× magnification. (B) Quantification of neuronal cell bodies to estimate cell density in myenteric plexus (\* $P = 0.0183$ ). (C) The number of cell bodies per ganglion in myenteric plexus. (D) The number of bridges in myenteric plexus. (E) Quantification of ganglions in myenteric plexus. (F) The number of bridges per ganglion in myenteric plexus (\* $P = 0.0253$ ). (G) Comparison of the number of cell bodies in the myenteric plexus between small intestine and colon (n.s., not significant).

## 국문초록

**배경 및 목적:** 오늘날의 최첨단 생체조직 투명화 기술은 조직 투명화와 항원-항체의 반응을 촉진시킴으로써 두꺼운 조직 또는 전 기관을 시각화 할 수 있게 한다. 본 연구는 위장관에 대한 조직의 2 차원 이미지보다 장신경계에 대한 정보와 통찰력을 더 많이 산출하는 3 차원 영상 방법을 개발하는 것이다. 이러한 접근방식은 염증성 장질환이나 장 운동성 장애와 같은 인간 질병에 대한 연구 목적과 진단에 대한 포괄적인 이해를 향상시킬 수 있으며 따라서 형질전환 쥐와 인간의 장신경계에서 베타 III 튜블린 (Tuj1), 신경성 산화질소 합성효소 (nNOS)와 콜린아세틸트랜스퍼라아제 (ChAT), 형광신경의 RNA 결합 단백질 (HuC/D)을 3 차원으로 시각화 하는 기법을 최적화하였다.

**방법:** 쥐와 사람의 소화기관 (식도, 위, 소장, 대장)을 시각화하고 정량화 하기 위해 다양한 기법으로 연구를 수행하였다. 고해상도의 3 차원 영상을 얻기 위해 쥐와 사람의 조직을 사용하여 조직 투명화 기법, 면역화학염색 (IHC), 공초점 현미경, 시트 형광 현미경 (LSFM)과 전체 위장관 두께에 대한 정량적 분석을 수반한 방법들이 개발되었다. 나아가 IMARIS 의 틀인 표면 렌더링, 모든 채널에 대한 볼륨 렌더링, 형광 임계치, 배경 제거 등을 사용하여 볼륨을 측정할 수 있는 정확한 3D 구조를 얻을 수 있었다.

**결과:** 쥐와 사람의 장신경계는 다양한 규모의 3 차원으로 시각화 되었다. 큰 조직에서 3 차원으로 면역염색과 이미징이 가능한 조직 투명화 방법은 근육층신경얼기, 점막하신경총과 점막 신경들의 네트워크를 보여주었다. 마찬가지로, 쥐의 식도 (16 × 14 × 5.3 mm) 와 사람의 대장 (1.2 × 1.3 × 1.4 mm) 조직 샘플에서도 3 차원 장신경 네트워크 구조를 잘 보여주었다. 쥐(n=3)를 사용하여 장 전체에 분포하는 ChAT 의 신경 구조를 연구하고, 두개의 주요 층에서 세포체와 신경절당 세포체를 정량화 하였다. 근육신경얼기의 연결도를 확인하기 위해 신경절의 수와 신경절과 신경절을 이는 다리도 측정하였다. 근육층신경얼기와 점막하신경총의 정량적 데이터는 비교적 서로 다른 양상을 보여주었다. 더 나아가 쥐에서 억제성 신경과 흥분성 신경을 면역 염색하는데 성공하였다.

**결론:** 이 연구는 쥐와 사람의 조직 투명화 기술에 적합하고 장신경계의 구조와 신경회로 연구에 적용 가능성을 높일 것이다. 특히, 콜린 작동성 뉴런의 수를 정량화하는 방법에 대한 검증을 제공한다. 쥐의 구조 표현형의 정량적 분석 방법은 진단 마커로서 이 기술의 잠재적인 유용성을 조명하고 장 운동성 장애의 경우 이 새로운 기술이 신경면역의 상호작용에 대한 광범위한 3 차원 네트워크 구조를 밝힐 것이다.

---

**주요어:** 조직 투명화, 장신경계, 근육층신경얼기, 점막하신경총, 3 차원 구조

**학번:** 2019-20007